Tools for Trapping and Detecting Ultracold Gases

by

Kahan M^{c}Affer Dare

B.Sc., The University of British Columbia, 2014

A THESIS SUBMITTED IN PARTIAL FULFILLMENT OF
THE REQUIREMENTS FOR THE DEGREE OF

MASTER OF SCIENCE

in

THE FACULTY OF GRADUATE AND POSTDOCTORAL STUDIES

(Physics)

THE UNIVERSITY OF BRITISH COLUMBIA

(Vancouver)

April 2016

Abstract

We construct a vertical imaging system designed to image along the quantization axis of the experiment. We demonstrate that it has a resolution on the order of 1-2μm which is on par with previous characterizations of the constituent components. We find that the inclusion of the vertical imaging system has a detrimental effect on the atom loading performance of the MOT. We show that this decrease is by approximately a factor of 2 down to 6.5×10^6 atoms per second and 8.1×10^7 atoms respectively. We subsequently detail the design of a novel lattice apparatus capable of tuning the lattice spacing by many orders of magnitude on the timescale of a typical experimental cycle. A proof-of-principle for this so-called dilating lattice is realized and the mechanism for variable lattice spacing is shown to work. Lastly, we cover our efforts towards measuring the effect of Feshbach resonances on collisional decoherence rates in ^{6}Li. To this end, we show that the Rabi frequency we can create given our current tools is approximately100Hz. A unknown strong mechanism for decoherence obstructs our experimental signature and a brief discussion of our attempts to discover its origin is presented.

Preface

This Master's thesis contains some of the author's research performed under the supervision of Dr. Kirk Madison at the University of British Columbia. The author has chosen to leave out their work concerning the construction of the experimental apparatus as well as their involvement in the spectroscopy of ^{6}Li, the measurement of Anomolous Autler-Townes splitting and the improvement on the 2-photon linewidth of the photoassociation light. Details concerning the construction can be found in William Bowden's Master's thesis [1]. A thorough discussion of the spectroscopic work, including the Anomolous Autler-Townes phenomena, is presented in William Gunton's PhD thesis [2]. As for the work concerning the narrowing of the 2-photon linewidth, the author has chosen to leave the reporting of those results to Gene Polovy out of respect for his work. This thesis instead focuses on the development of both a new imaging system and a novel lattice system. Michael Kinach was instrumental in the design of the mount for the imaging optics and its subsequent characterization discussed in Chapter 2. The dilating lattice system described in Chapter 3 was built together with Kai Ogasawara. The experimental apparatus used in Chapter 4 was built in collaboration with William Bowden, Will Gunton, Mariusz Semczuk, Gene Polovy, and Koko Yu.

Table of Contents

List of Figures

Acknowledgments

Growing up in this lab, I learned more than I could have ever anticipated. Looking back, I couldn't have done it without all of the discussions and laughs I had with the great people of our lab. The open and free atmosphere that my supervisor, Dr. Kirk Madison, has cultivated in our lab lead to a comfortable and relaxed environment. I will forever be grateful for the opportunity to pursue my own interests and voice my opinions as this has helped me mature as a researcher and a person.

Making the transition between the well-structured undergraduate life and the independent graduate life was made easy thanks to my peers that helped me along the way. The long nights spent working with William Bowden showed me what real dedication and commitment are like. His relentless yet friendly demeanour has stuck in my mind as a goal to strive towards.

Of course, I wouldn't have been able to do much research without the mentorship of Will Gunton. From my first day to my last, Will has consistently pushed me harder than anyone else to embody the spirit of a researcher. With his guidance, I have not only learned to build and run our experiment, but also to trust myself.

Whenever I got tired or frustrated I could complain to my friends, and fellow Masters students, Koko and Kais. Whether it was classes, help figuring out problems with our experiments or just random discussions, Koko and Kais were always there when I needed them.

To Mariusz, I only wish you could've stayed in our lab for longer. I always enjoyed our talks about crazy experiments you were thinking up. One of the friendliest fellows I will ever meet, you could always make us laugh no matter how tired or frustrated we were with the experiment. I can't thank you enough for all that you've done for me and I wish you the best in Poland.

I couldn't have asked for a better partner in crime than Gene Polovy. Forever playing the devil's advocate, I couldn't be more grateful for my friendship with this magnificent fellow. Working together with him these past couple of years has been a pleasure and I can only hope that someday he realises that my hook idea is genius.

Lastly, to my soon-to-be wife Zoya. I don't know how you've put up with me throughout my degree, let alone the past 7 years. The nights where I had to stay all-night would've been terrible had it not been for your lovely care packages. I'm glad that we could go through all of this together and look forward to continuing along this journey with you.

Chapter 1

Introduction

We will start the thesis with describing the author's personal motivation for pursuing research in the field of ultracold physics before discussing what advantages ultracold physics has when it comes to studying certain topics. This will lead to a more focused motivation for, and introduction of, the current experiment and the work presented here.

1.1 Motivation

As our understanding of physics progresses, so too do the problems we face. These questions we seek to answer become more numerous and what we call physics grows and diversifies, slowly creating more subfields. In my opinion, one of the most interesting perspectives one can have on physics is comes when one straddles multiple subfields, transcending traditional knowledge boundaries. After all, everything is physics and these distinctions between nuclear, condensed matter, high energy, etc. are in no way hard boundaries.

This perspective is why I am drawn to these ultracold experiments. By their very nature, they act as clean testing grounds for researchers to pursue a variety of topics. Using the tools developed in the field of Atomic, Molecular and Optical (AMO) physics, one can study a large range of topics: the gravitational redshift [3], parity violating effects [4], EPR pairs [5] Kondo physics [6], precision spectroscopy [7, 8], and topologically protected quantum qubits [9] to list a few. This is by no means an exhaustive list and but the depth and breadth are impressive, especially considering it is only a couple of decades old. It is this variety that motivates to me as it encourages a broader perspective by allowing physicists to consider problems outside one's realm of expertise.

The experiment we are currently pursuing is the formation of ultracold LiRb molecules in their lowest lying triplet state. The motivation for this experiment lies in the recent realization that atoms in lattices can be used to systematically engineer various types of Hamiltonians [10]. Even more compelling is the proposal for using polar molecules in a lattice to simulated any permutation-symmetric two-spin-1/2 interaction[9]. The mechanism by which this works requires the molecules to have both an electric dipole moment (EDM) and a magnetic dipole moment to be able to create such anisotropic interactions.

This flexibility and applicability of a single apparatus is a strong motivator, from an experimental standpoint. to construct such a system. The polar molecule we have chosen to pursue is LiRb which has an electric dipole moment (EDM) of ~ 4.15D[11–13]. Other heteronuclear molecules like KRb and LiCs are also attractive options and have been formed by Dr. Jun Ye and Dr. Debbie Jin's groups [14] and Dr. Matthias Weidemüller's [15] groups respectively. LiRb was chosen due to the strong knowledge of both species within the group.

1.1.1 Why ultracold?

One might question the need for particles to be ultracold in order for researchers to study the topics mentioned above. After all, our lab is called the Quantum Degenerate Gases laboratory and yet degenerate Fermi gases exist at temperatures over 10^5K in the form of white dwarves, dense stars near the end of their lifetime. While it is true that one does not need to be in the ultracold regime to study such topics, it is extremely beneficial as it provides a new approach to examining these systems. To study the physics governing many aspects of a white dwarf, one need not create a star in the lab for probing but instead an ultracold plasma [16].

For instance, it has been shown that that the Hubbard model, which is believed to explain unconventional superconductivity, is impossible to solve analytically or computationally. Various solutions have been posited under various approximations but we still don't have a complete picture as to the mechanisms behind unconventional superconductivity. By trapping ultracold atoms in optical lattices, physicists believe they can probe the Hubbard model in a precisely controlled manner. In fact, Dr. Randall Hulet's group has managed to observe antiferromagnetic correlations in the Hubbard model using ^{6}Li at a temperature of ~ 30nK [17]. It is believed that by further decreasing the temperature by an order of magnitude, one should see evidence of D-wave pairing, giving condensed matter physicists key insight into one of the outstanding problems in physics today.

There are many more examples where lowering the temperature gives researchers access to phenomena that are usually at too low of an energy scale to probe via other methods. This flexibility is supported by the many tools that have been developed over the past couple of decades to confine and control atoms.

While various forms of traps have been developed, a more striking feature of ultracold physics is the ability to tune interaction strengths between particles. This tuneability most often comes in the form of Feshbach resonances whereby one can tune the scattering length across a resonance simply by tuning the magnetic field in which the particles are held. The details of this phenomena are discussed in great detail in [2] but it suffices for our motivation to simply realize the experimental simplicity of this effect. One can suppress interactions, cause them to be attractive or repulsive, or some mixture in between if one considers the difference in the interactions between atoms of varying internal states, all by tuning the magnetic field.

1.2 Overview of the Experiment

The most common way to prepare ultracold atoms is to start with some form of laser cooling. Consider, for instance, an atom moving along the z-axis. If one were to shine a near resonant, red-detuned laser along the z-axis, counter to the motion of the atom, then the laser's frequency will be Doppler shifted to a higher frequency. If the detuning is picked such that the Doppler shift shifts the laser into resonance then the atom can absorb a photon. The now excited atom will be moving slower to conserve momentum and after some time it will reemit a photon. However, this emission will be isotropic meaning that on average the change in momentum due to the emission of photons will be zero. This means that the atom will have been slowed down by the laser. If this is now done in an ensemble of atoms, the temperature will have decreased. This is the principle behind laser cooling.

Unfortunately, laser cooling molecules is not as easy because their complicated internal structure makes it difficult to make sure all of the atoms stay in the state which will be Doppler shifted correctly. Since this is one of the main tools in the AMO toolbox, for achieving ultracold temperatures, it makes an already involved experiment significantly more challenging. An alternative approach is to cool the constituent atoms to ultracold temper-

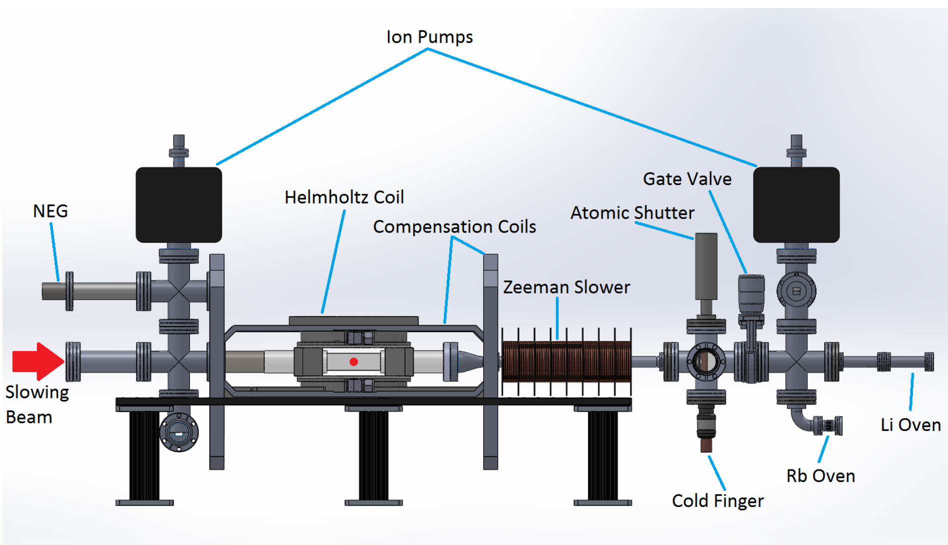

Figure 1.1: A SolidWorks drawing of the major components of the experimental apparatus. For reference, the part of the apparatus to the left of the gate valve will be called the science section while the section to the right will be the source section. Differential pumping separates the two sections, allowing the science side to operate at a pressure of $\sim 5\times10^{-9}$torr. An atomic shutter can be controlled electronically to block the direct path between the source and science sections. Not pictured here are the compensation coils, the vertical imaging apparatus and optics. More detailed descriptions can be found in [1, 2]

atures before pairing and transferring them to the desired molecular state. We have chosen to pursue the second method and the main steps for doing so are as follows: trap and cool Li and Rb atoms, transfer the atoms to an optical lattice, pair the atoms together and transfer to a molecular state.

To elaborate, we must first discuss the current experimental apparatus shown in Figure 1.1. The sources of our atoms are two chunks of metal (one for each species) which are heated up to hundreds of degrees Celsius. At these temperatures, some portion of the metals are converted to a gaseous phase before they exit the source chamber and travel down the axis of the experiment towards the science side. The atoms in these gases are moving at hundreds of meters per second which is far too fast to catch in any of our traps. Hence, we employ a so-called Zeeman slower [18] to decrease the velocity of the atoms down to captureable velocities for our Magneto-Optical Trap (MOT). These atoms are then cooled in the MOT via Doppler cooling down to temperatures on the order of ~ 100μK. These atoms are then transferred to a Crossed Optical Dipole Trap (CODT) before being evaporated further down to anywhere from ~ 100nK-10μK [19].

In this current iteration of the experiment, we have achieved the first step for creating LiRb molecules. The method for pairing Li and Rb atoms is tuning their interactions via the previously discussed Feshbach resonance so that that it is effectively attractive. We have previously observed these Feshbach resonances [19, 20] so all that is left is trapping the atoms in an optical lattice and ultimately forming molecules. We are currently focusing on the latter, using only Li (forming Li_2 molecules) as a testing ground for our experimental techniques. The method that we hope to utilize is called Stimulated Raman Adiabatic Passage (STIRAP) which uses two coherent laser pulses to adiabatically transfer atoms between two states via some third intermediate state.

The reason we are taking this intermediate step is two-fold. First, when the experiment was first built, there was no high resolution spectroscopic for LiRb while Li_2 was well studied, making it an ideal benchmark for a brand new apparatus. Second, before this experiment, Li_2 had only been well outside of the ultracold realm, which means there is still interesting science to be done. We therefore sought to create deeply bound Li_2 molecules as quantum degeneracy of such molecules had never before been achieved.

1.3 Overview of this Thesis

Chapter 2 discusses the theory, design and implementation of a vertical imaging system for increasing the detection efficiency of the current experimental apparatus. As we believe we will be producing, at least initially, a small number of molecules, increasing the signal to noise ratio (SNR) of our detection scheme is of paramount importance for the development of our molecular formation techniques. A review of the initial work towards this end [21] will be presented. The optomechanical constraints are discussed as well as the consideration of a vertical lattice. A preliminary characterization of the vertical imaging system is subsequently presented as well as the proposed method for a more final verification of the resolution.

Next, our efforts towards the realization of a novel lattice scheme will be discussed in Chapter 3. We start with a discussion of interference and the possible lattices spacings one can achieve for a given apparatus. This leads us to detail the various iterations of our design before we present our final design for the dilating lattice system. The realization of this design will then be examined, resulting in a thorough breakdown of the difficulties associated with building such a lattice. Finally, the merits and design for a monolithic container are presented as a way to improve the portability and applicability of the system.

Lastly, in Chapter 4, we will report on our preliminary work focused on a measuring the effect a Feshbach resonance has on collisional decoherence rates. We discuss the theory behind Rabi oscillations and adiabatic passage before discussing these concepts as experimental tools. We outline our experimental procedure for using Rabi oscillations between hyperfine states in ^{6}Li to detect the rate at which decoherence occurs due to collisions between hyperfine states. We discuss some obstacles we encountered in trying to realize this proposal, and some open questions about the performance of our RF spectroscopy equipment.

Chapter 2

The Vertical Imaging System

While the current iteration of the experimental apparatus utilizes a camera positioned horizontally as shown in Figure 2.1, the development of a second imaging system aimed along the vertical axis, parallel to the magnetic field, has become critical to our goal of creating ultracold polar LiRb molecules. The reason for this is twofold: the increase in resolution, and the ability to properly image at high magnetic fields. Since we expect, at least initially, to be creating small numbers of molecules, we are aiming to increase our signal to noise ratio (SNR) in order to amplify our weak signal.

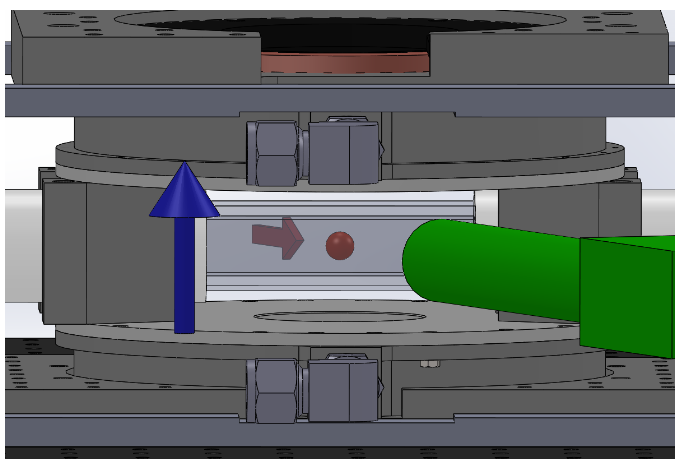

Figure 2.1: A depiction of the current imaging geometry. The green object depicts the current imaging systems orientation in the horizontal plane of the experiment. The blue vertical arrow labels the orientation of the magnetic field due to the Feshbach coils. The red arrow shows the direction in which the absorption imaging beam propagates while the red sphere in the middle of the cell notes the location of the atoms.

2.1 Theory

One of the most common methods for acquiring data in ultracold atom experiments is via some form of imaging. Once calibrated, images provide a straightforward method for determining spatial densities of cloud of atoms. It is also an extremely adaptable method as the manner in which the cloud is prepared for the image can drastically change the outcome. For instance, the imaging light can be prepared in such a way that it only interacts with a certain atomic state, giving rise to state selective imaging.

Another common technique, which is often times used for measuring the temperature of a cloud of atoms, is time-of-flight imaging. Instead of imaging the atoms while they are confined in some trapping potential, one turns off the trap allowing the atoms to freely expand. To understand what happens let us label the initial state of the atoms by $|\Psi(t=0)\rangle$ which has some characteristic width L. Then if we time evolve the associated field operator $\hat{\psi}^\dagger(x, t=0)$ we find that

$$\begin{aligned}\hat{\psi}^\dagger(x,t) &= \hat{U}^\dagger(t)\hat{\psi}^\dagger(x,t=0)\hat{U}(t), \\ &= \int_{-L/2}^{L/2} dx'\hat{\psi}^\dagger(x',t=0)\int \frac{dk}{2\pi} e^{i[k(x'-x)-\omega(t)t]}, \qquad (2.1) \\ &= \int_{-L/2}^{L/2} dx'\hat{\psi}^\dagger(x',t=0)\mathcal{I}(x'-x,t), \qquad (2.2)\end{aligned}$$

where

$$\mathcal{I}(x,t) = \int \frac{dk}{2\pi} e^{i[kx-\omega(k)t]} \approx \sqrt{\frac{m}{2\pi it\hbar}} e^{i\frac{mx^2}{2t\hbar}} e^{-i\pi/4}. \qquad (2.3)$$

Now if we imagined L were infinitesimally small then after some time each particle would classically be at a position given purely by its velocity and the travel time. Therefore, if the momenta of the particles were quantized, one would see shells of whose separation would be governed by the associated velocities and the expansion time. Now if the cloud originally had some finite size then these shells would be blurred so one can naturally ask the question of how long does one need to let the cloud expand to resolve these momentum shells. To see this, we return to our example, taking now the commutator

$$\left[\hat{\phi}_k, \hat{\psi}^\dagger(x,t)\right] = \int_{-L/2}^{L/2} dx' e^{-ikx'} \mathcal{I}(x'-x,t) \approx L \exp\left(-i\frac{2t\hbar\pi^2k^2}{m}\right) \mathrm{sinc}\left(\frac{mxL}{2t\hbar}\right). \tag{2.4}$$

where we have assumed that $x >> \frac{L}{4}$. This is a valid assumption as we're concerned with the case where the cloud has expanded to be much larger than its original size. From the sinc term, we can see that the characteristic width of this new distribution is $W = \frac{2\pi t\hbar}{mL}$. Given our assumption of the clouds expanded size, this requires an expansion time $t_{\mathrm{TOF}} >> \frac{mL^2}{8\pi\hbar}$. For a trapped Li cloud of size 20μm, we find that $t_{\mathrm{TOF}} >>$ 1.5ms which is a feasible time expansion time for our experimental system. Hence, a simple modification to normal imaging allows us to determine the momentum space density which naturally leads to temperature information.

Given these couple of examples we will proceed with discussing the two main methods for taking images of atoms. The first, absorption imaging, revolves around the scattering of light away from the camera, casting a shadow on the detector that one can then use to infer the spatial density of the atomic cloud. This is the type of imaging we will be concerned with in discussing the imaging system.

2.1.1 Absorption Imaging

Absorption imaging is a popular imaging method as the atomic cloud need not be held in place while the image is being taken. This means it can be used to take time-of-flight measurements for instance. While the versatility is a strong benefit, it is heavily dependent on the atomic scattering rate which is defined by

$$\Gamma = \frac{\Gamma_0}{2} \frac{s}{1 + s + (2\delta/\Gamma_0)^2} \tag{2.5}$$

where $s = I/I_s$ is a parameter which determines how close one is to saturating the transition, Γ_0 is the bare scattering rate and δ is the detuning of the light from a given transition. For most of our purposes, we can simplify this equation by taking $(2\delta/\Gamma)^2 \approx 0$, $s \approx 1$ and $\Gamma_0 \approx$ 6MHz for ^{6}Li. This means

$\Gamma \approx 1 - 2\text{MHz}$.

One then needs to compare this to the relevant noise levels in the imaging system. One inevitable source is shot noise. This simply comes about due to the fact that light now acts like particles and their very discrete nature means they have an uncertainty governed by the Poisson distribution. For large numbers of events, the standard deviation of shot noise approaches the square root of the number of events and therefore we can define a signal to noise ratio (SNR) as

$$\text{SNR} = \frac{\Gamma \cdot t \cdot \text{QE}}{\sqrt{A \cdot I \cdot t \cdot \text{QE}}} \tag{2.6}$$

where t is the exposure time, QE is the quantum efficiency of the imaging apparatus, I is the intensity of the light in photons per second, and A is the area of a particle's possible position. As can be seen in Figure 2.2, there is a maximum in the SNR as a function of s and one can show it occurs when

$$s = 1 + \left(\frac{2\delta}{\Gamma_0}\right)^2. \tag{2.7}$$

The exposure time is effectively limited by the atomic drift, especially

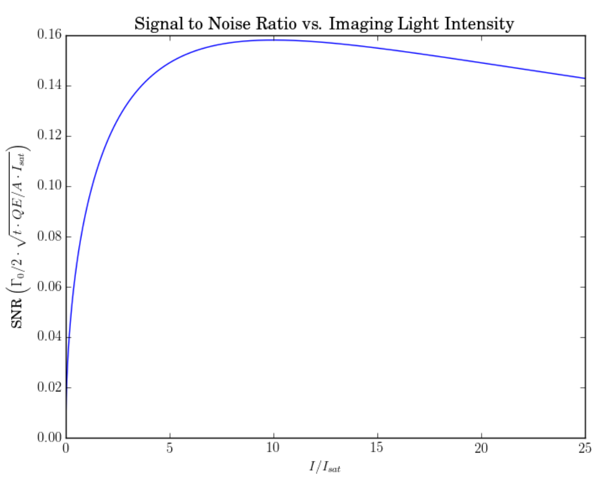

Figure 2.2: A plot of Equation 2.6 using $\delta = 10\text{MHz}$, $\Gamma_0 = 6\text{MHz}$ which are standard values for ^{6}Li.

when one is concerned with light species. For instance, given a sample of ^{6}Li trapped at 10μK, the average velocity will be on the order of 0.1m/s which means if one were to expose the atoms for even 0.5ms, the atom will have moved 50μm which is larger than the size of our dipole trap (which is on the order of 30μm). Hence, this would erase all spatial information. This is also not considering the recoil velocity imparted on the atoms by the imaging photons, which at this is also approximately 0.1m/s. In order for images to retain their spatial information, one needs to at least decrease the exposure time such that the atoms only scatter photons within some small spatial region on the order of the resolution of one's imaging system.

One should note that inverse relationship between the SNR and $\sqrt{A}$. While A is not usually a tuneable parameter, this relationship motivates using a pinning lattice to confine atoms to a well defined position. To estimate the difference on the SNR for a lattice and a dipole trap one simply needs to consider the characteristic size of each trapping potential. For a normal 1064nm lattice and our dipole trap which is approximately 30μm in diameter, this ratio is approximately $(30\mu\text{m})^2/(1064\text{nm}/2)^2 \approx 3000$. As the quantum efficiency is usually anywhere between $5\% - 90\%$, we see that this change between imaging atoms in a dipole trap as opposed to a lattice makes the most dramatic change in the SNR out of all of the parameters.

For our current experiment, we are planning to use the Point Grey FL2G-13S2M-C which has a quantum efficiency of $\sim 40\%$ at 671nm (Li light) and 30% at 780nm (Rb light). For comparison, the Andor iXon Ultra 888 has 80−90% at these wavelengths. This improvement would be great but the cost of these products scales dramatically as one approaches a quantum efficiency of 100% and since the SNR only scales like $\sqrt{\text{QE}}$, one should consider if this improvement is worth the expense.

One other aspect to consider when looking at cameras is their dark current. This is another source of noise due to the small amount of current that flows through the device even when no photons are being registered. Fortunately, for the case of CCD cameras, this noise is negligible and we can ignore it. It can be a significant problem for other types of detectors like near-IR detectors.

2.1.2 Fluorescence Imaging

The main alternative to absorption imaging is fluorescence imaging whereby atoms absorb light and re-emit it in a different direction. The emission light can be collected along some axis and the image will be bright if there is a high density. Since the captured solid angle is relatively small, the number of photons that scatter towards the camera is low, requiring that the cloud be exposed for a large duration to build up a detectable signal. These long durations allow for atoms to drift and so one needs to confine them in order to take an image. Some standard traps for this are MOTs or pinning lattices whereby the new limiting factor is the timescale on which atoms would heat out of the trap.

2.1.3 High-Field Imaging

Atomic imaging relies on light being scattered and therefore that your imaging light is resonant, or at least close to resonant, with some atomic transition. It must also be of the correct polarization to satisfy the dipole allowed transition selection rules. As such, imaging light at low magnetic fields and high magnetic fields might have to be different and indeed that is the case with ^{6}Li.

At zero magnetic field, we image on the $|F = 1/2\rangle \to |F' = 3/2\rangle$ transition which counts all of the atoms since both the m_F projections are degenerate. At small magnetic fields, hyperfine splitting causes us to select one of the two m_F states to image meaning our effective SNR is decreased. Furthermore, as we increase the magnetic field, F and m_F are no longer good quantum numbers and replaced with m_J and m_I. As is shown in Figure 2.3, the levels separate into $m_I = -1, 0, 1$ triplets with different m_J numbers. We usually focus on imaging the $|1\rangle$, $|2\rangle$, and $|3\rangle$ states, which have $m_J = -1/2$ and $m_I = 1, 0$, and -1 respectively, using the $m'_J = -3/2$ excited states. As we will soon show, at high fields this transition is closed, allowing us to forgo a repump beam. However, there is still a differential Zeeman shift which is approximately linear past 100G and can be written as

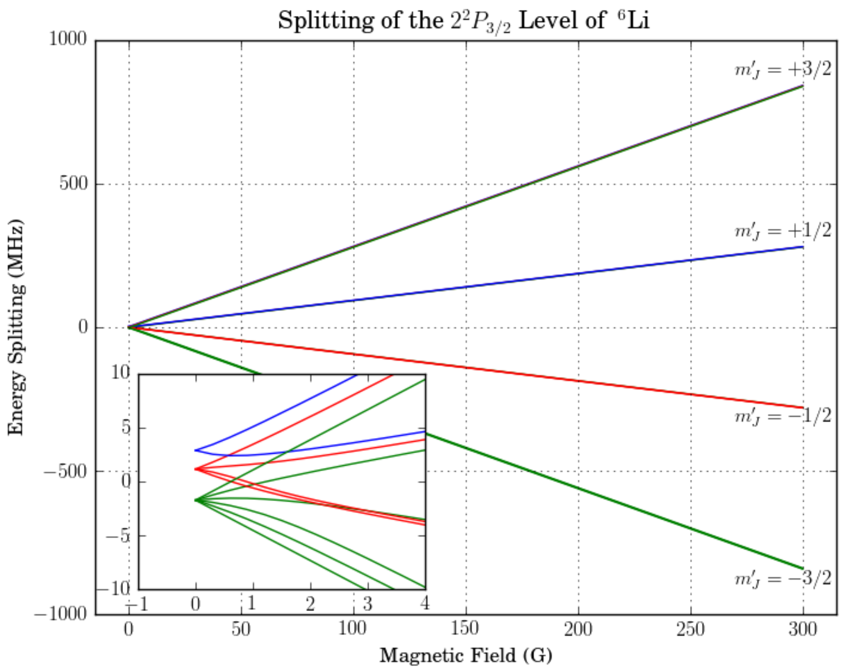

(a)

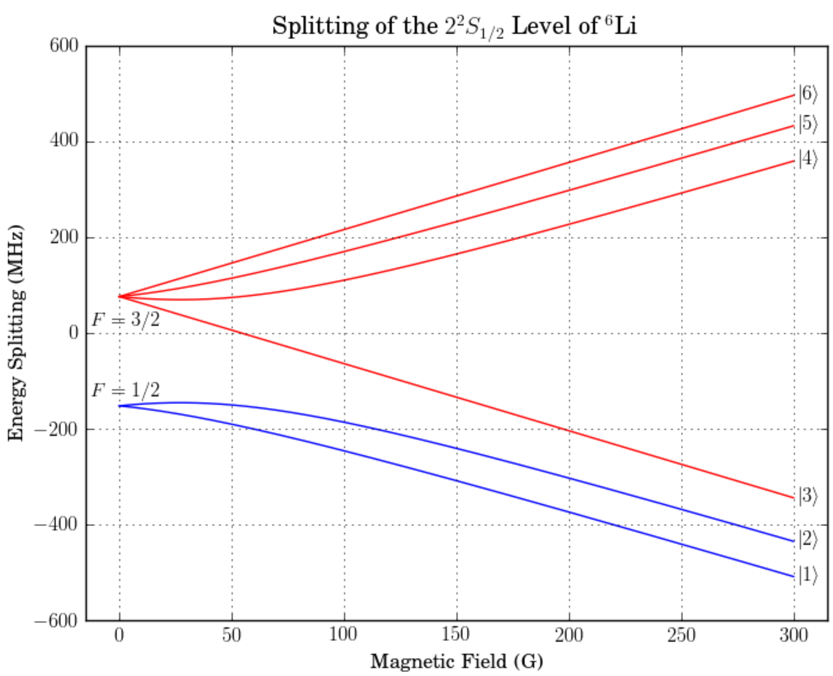

(b)

Figure 2.3: The effect of magnetic field on the $2^2\mathrm{P}_{3/2}$ level of ^{6}Li is shown in (a) and on the $2^2\mathrm{S}_{1/2}$ level in (b). Note that in (a), the blue levels split from the degenerate $F' = 1/2$ manifold while the red from the $F' = 3/2$ and the green from the $F' = 5/2$.

$$\delta_1 = -1.4\text{MHz/G} \cdot B + 158\text{MHz}, \tag{2.8}$$

$$\delta_2 = -1.4\text{MHz/G} \cdot B + 82\text{MHz}, \tag{2.9}$$

$$\delta_3 = -1.4\text{MHz/G} \cdot B. \tag{2.10}$$

where δ_i is the detuning of the transition $|i\rangle \to |m_J' = -3/2\rangle$.

This large frequency shift requires us to have a second laser system for generating the high-field imaging light and this is described Dr. Semczuk's thesis [22]. Here we will focus more on the consequences of the hyperfine splitting rather than discussing the laser system.

Due to the splitting, one has to be careful of atoms decaying to a state which is transparent with respect to the imaging light as they will no longer contribute to the image. To understand how this might happen, we look at a simplified 6 level system shown in Figure 2.4. The selection rules that govern which transitions are allowed are simply $\Delta m_J = 0, \pm 1$ and $\Delta m_I = 0$ (the latter is what lets us only consider the 6 levels as each one is triply degenerate with $m_I = 0, \pm 1$). In this case, we see that only the $m_J' = \pm 3/2$

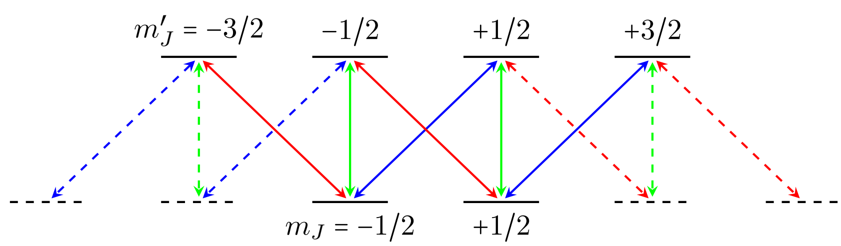

Figure 2.4: A diagram for illustrating the relationship between various transitions and their required polarizations of the coupling light. Note that this is not meant to describe the energies of the states and one should consult Figure 2.3 if one is looking for that information. Furthermore, each level here actually represent a triplet with $m_I = 0, \pm 1$. The green, red and blue transitions are those driven by π, σ_-, and σ_+ polarized light respectively. Dashed transitions are those that a disallowed due to the lack of a level (shown as dashed levels). Note that any transition to either the $m_J' = \pm 1/2$ will not be closed due to there being two allowed decay channels. On the other hand, the only allowed transitions to the $m_J' = \pm 3/2$ are closed as there is only a single decay channel which returns the atom to its original state.

states have closed transitions as they can only decay to the state which the light is resonant with. As our atoms start in the $m_J = -1/2$ states, this means the closed transition we are left with is $m_J = -1/2 \to m'_J = -3/2$ transition. Therefore, we require our light to be circularly polarized to conserve angular momentum.

In order for the particles to see purely right- or left-handed circularly polarized light, the light must propagate along the quantization axis of the atoms. It is at this point that the orientation of our system is important. The magnetic field, generated by our Helmholtz coils, defines the axis of quantization to be along the vertical axis, as depicted in Figure 2.1. Hence, an imaging system aligned along the vertical axis is required in order for the imaging light to efficiently interact with the gas cloud.

At present, the system is aligned horizontally as shown in Figure 2.1. Light that is polarized in the plane perpendicular to the quantization axis will have its polarization vector project onto the quantization axis, creating and even superposition of right- and left-handed circularly polarized light. These different circular polarizations will then drive σ_+ and σ_- respectively. Alternatively, one can drive π transitions by having light polarized along the quantization axis. Since we wish to drive σ_- transitions though, we are forced to linearly polarize our light in the plane perpendicular to the quantization axis. This results in the highest scattering rate for this orientation, however this means that each atom only interacts with half of the photon due to the even split in polarization. This causes a severe undercounting of the number of particles in the trap because much more light passes through the cloud than one might expect. One can correct for this undercounting in one's analysis, however when one is working with small atom numbers other sources of noise can become comparable to the signal one is looking for. This can't be corrected for in the analysis and therefore correcting for this undercounting by imaging along the quantization axis becomes important for imaging small samples.

2.1.4 Imaging Resolution

As we have decided to build a new imaging system we aimed to create a system that would be able to have single-site imaging capabilities for a reasonably made lattice without spending an exorbitant amount of money. Our current plan is to build a lattice with a periodicity of $1 - 2\mu$m and at these scales, the resolution of such a system is most likely diffraction limited. When one is intending to image anything with great fidelity, one starts thinking of how well your image will mirror your object. As is with all waves, diffraction will cause a blurring of edges in a realistic imaging system.

To illustrate this, we will calculate the impulse response function of the system shown in Figure 2.5. The impulse can be described as a spherical wave and thus, in the aperture plane, it can be approximated as a paraxial

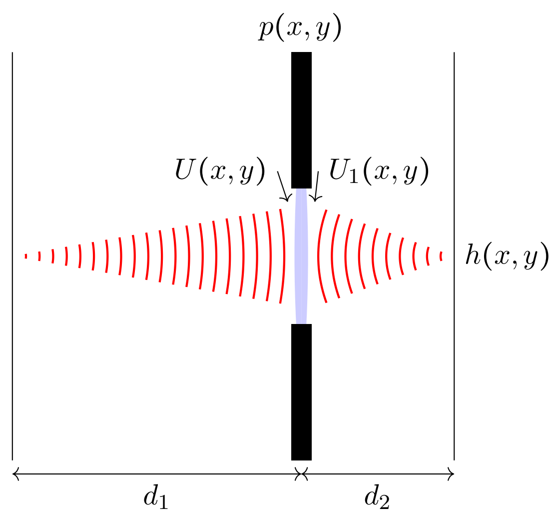

Figure 2.5: A standard diagram for a finite sized lens. We model the lens itself as an infinite lens but overlay it with an aperture, causing diffraction in the light.

wave. Therefore, in the aperture plane it has a complex amplitude given by

$$U(x,y) \approx U_0 \exp\left(ik\frac{x^2+y^2}{2d_1}\right). \tag{2.11}$$

After transmitting through the aperture and lens, it is now described by

$$U_1(x,y) \approx U(x,y)\exp\left(-ik\frac{x^2+y^2}{2f}\right)p(x,y) \tag{2.12}$$

where

$$p(x,y) = \begin{cases} 1 & : \sqrt{x^2+y^2} \leq R \\ 0 & : \text{otherwise} \end{cases} \tag{2.13}$$

is the transmission function of the aperture and R is the radius of the aperture. If one then propagates this to a distance d_2 which satisfies the imaging equation, then we get that

$$h(x,y) = U_0 \frac{J_1(2\pi R\rho/\lambda d_2)}{\pi R\rho/\lambda d_2} \tag{2.14}$$

where $\rho = \sqrt{x^2+y^2}$ and $J_1(x)$ is the first order Bessel function. This intensity distribution is called an Airy pattern. The first zero-crossing of this function occurs at $\rho_{\min} = 1.22\lambda d_2/2R$ which gives a natural scale for the resolution of your system. The so-called Rayleigh criterion for distinguishability requires that for two points to be resolved, one must have the separation of their respective Airy patterns satisfy $\rho \geq \rho_{\min}$. Put another way, this states that the maxima of the Airy patterns created by two point sources must lie outside of the others' first zero-crossing. Assuming one were to image an object at infinity, this criterion simplifies to

$$\rho \geq 1.22\lambda F_{\#} \tag{2.15}$$

where $F_{\#} = f/2R$ is the F-number. Therefore, one wants as small an F-number as possible to increase the resolution of the system. Getting a large lens can help with this as well as decreasing the focal length.

Unfortunately, in reality there are other effects that further limit the resolution of one's system. Two very common types of aberration are chromatic and spherical aberration.

Chromatic aberration happens when different wavelengths of light focus at different positions. As a consequence of this, the imaging apparatus must be aligned separately for each ^{6}Li and Rb since the depth of focus will be on the order of the size of our atomic cloud. While this is unfortunate it also means that chromatic aberrations won't impact our resolution since we'll only be using a single frequency of light at any given time.

Spherical aberration, on the other hand, is a significant problem since it is inherent in almost all lenses. It is caused by the increased refraction of light rays that strike the outer regions of the lens compared to the center. This results in the rays focusing at different points depending on where they hit the lens as depicted in Figure 2.6.

One can mitigate this effect by using a complex system of lenses, a specially designed aspheric lens or an aperture. As our objective is to produce an imaging system on a reasonable budget, we focus on utilizing the second two options as they don't require any costly components and are also rela-

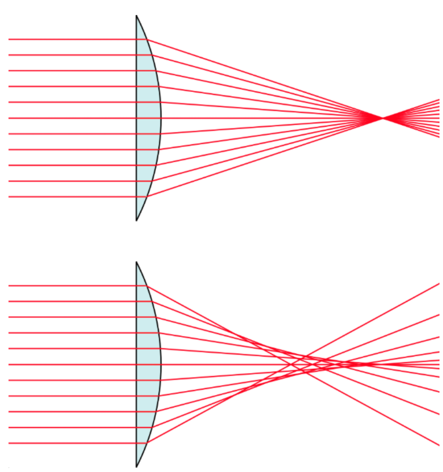

Figure 2.6: The top image is an example of what the rays would look like if there was no spherical aberration. The bottom image depicts a lens with spherical aberrations where the rays focus at varying positions along the horizontal axis.

tively simple to implement. By placing the aperture at the Fourier plane, one can block the rays that aren't focused at the focal plane. In principle, one can continue to aperture down until all but the perfectly focused rays are let through and hence get rid of all of the aberrations.

In practice, there is some trade-off between reducing the spherical aberrations and decreasing the resolution which will limit how much of the aberrations can be eliminated. This limit can be found experimentally as it will depend on each individual system. In certain systems, one can forego this filtering and attempt to correct for the spherical aberrations in the analysis, however it presents significant complications when looking at correlations in an image. This is because the distortion in the image will cause deviations away from the true intensity of the pixels, which then can cause false correlations to arise. These confounding artefacts are particularly harmful when looking at small fluctuations in the image which is how one tests for entanglement as detailed in [6].

2.2 Design

A thorough discussion of the basic design and characterization of the components of the imaging system was done in my undergraduate thesis [21] and I will only present the considerations we undertook when designing this system as well as the final design.

2.2.1 Considerations

While designing an imaging system comes with its own inherent difficulties, our main constraints were due to the fact that the imaging system had to fit into an already built experiment. Furthermore, we had planned to add a lattice along the vertical direction of the existing apparatus, complicating the design further. Given the geometry of our experiment, shown in Figure 2.7, we can see that the size of the lens must fit inside a 60mm cylindrical section, limiting R. We then seek to place the lens as close to the cell as possible and will henceforth discuss the restrictions on the lens placement.

The major complication arises due to the fact that not only is the imaging light and the lattice light travelling along the vertical axis, but the vertical MOT beam as well. This makes things more challenging as the MOT beam and imaging light are only detuned from one another by tens of megahertz and there are no available dichroic mirrors that have such a sharp cut-off at 671nm.

Hence, one needs to separate the imaging and MOT light from the lattice light and then separate them from one another. While this is normally not difficult, the imaging lens will focus the MOT beam, causing it to subsequently diverge and therefore this diverging beam must be recollimated after the imaging beam is separated. This means that one has a path length of ~ $2f$, where f is the focal length of the imaging lens, to have the imaging and MOT beams completely separated. To increase our resolution, we want

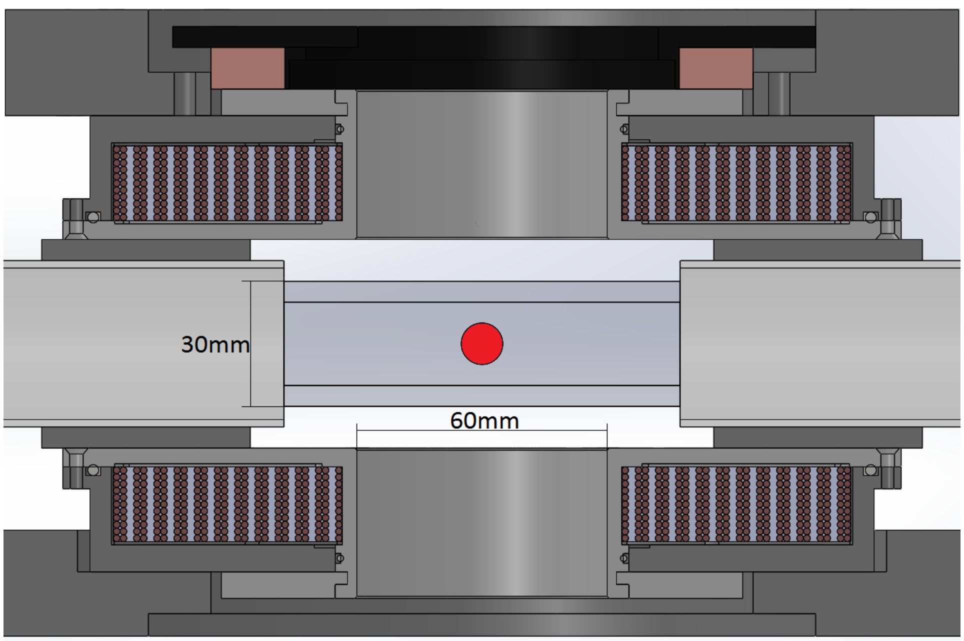

Figure 2.7: A cross section of the science section of the experimental apparatus. Here the red dot signifies the location of a trapped cloud. Note the cylindrical regions directly above and below the clouds position are empty and are there to allow for optical access along the vertical axis.

to make f as small as possible so optimizing these parameters was the main consideration.

The lab had previously purchased the ThorLabs AL5040-B 50mm lens with imaging in mind. This lens happened to have a focal length that closely matched what was possible for the imaging system to tolerate given its criterion. As such the lens, as well as other key components, were characterized as part of my undergraduate thesis and basic design for the lens mount, shown in Figure 2.8, was made. This design would be attached to a 3-axis translation stage for precise alignment. The dichroic mirror is meant to separate the imaging and MOT beams (which are reflected) from the lattice beams (which are transmitted). A quarter waveplate and polarizing beam splitter would be placed right after the circular aperture in the bracket to separate the imaging and MOT beams.

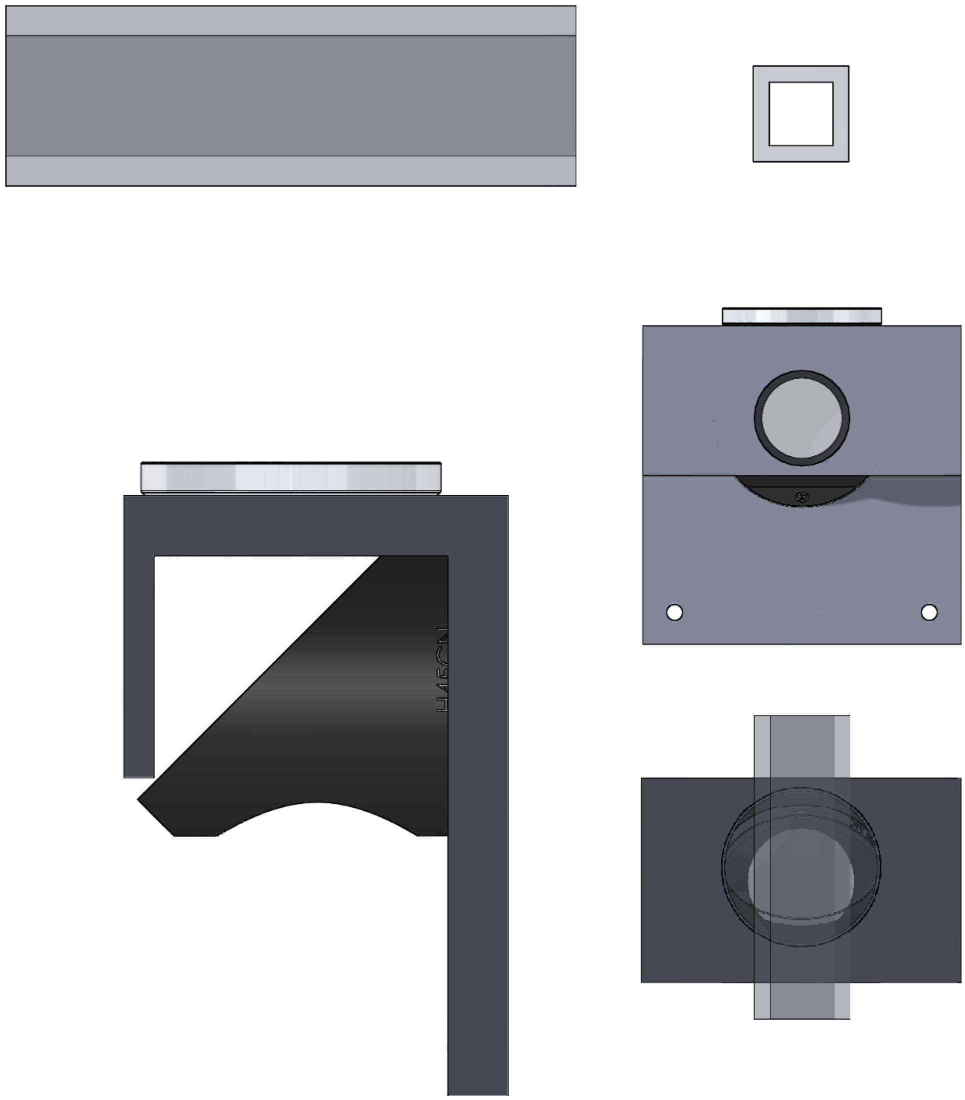

Figure 2.8: A Solidworks drawing of the basic lens mount. The cell is depicted as being stationed above the entire mount with the lens resting in a round hole. Inside the bracket part is a Thorlabs H45CN 45° mount holding the dichroic mirror.

2.2.2 Construction

From the rather basic imaging mount design shown in Figure 2.8, we worked to build one monolithic mount to hold most of the imaging optics securely. This final design, shown in Figure 2.9 contains all of the separation optics. This mount is actually made up of 4 major pieces shown in Figure 2.10, upon which various optical elements are secured. For more details about the imaging mount, one should refer to Michael Kinach's report.

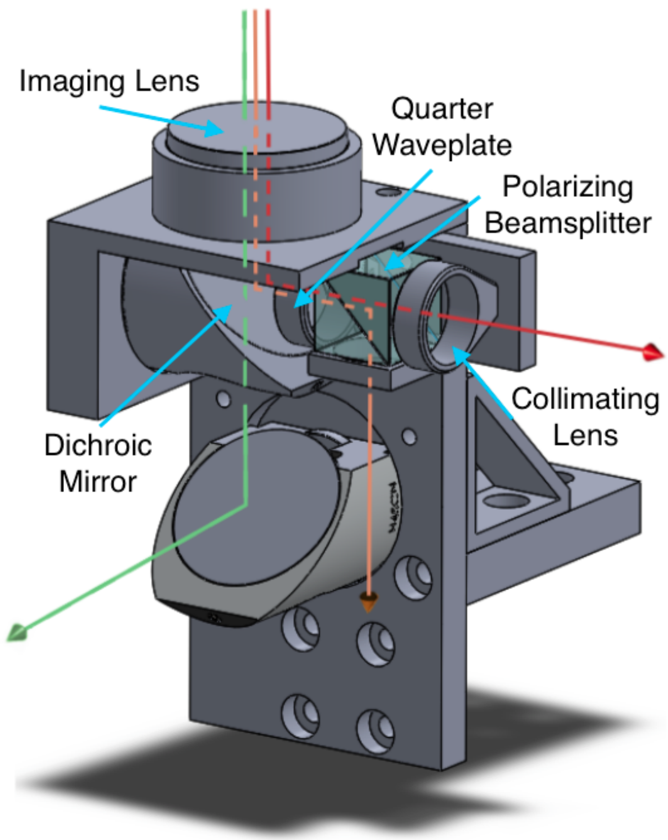

Figure 2.9: The final imaging mount design. The green arrow labels the path of the lattice beams, the red arrow is the path of the MOT beam and the orange is the path of the imaging light. This mount will fit on a 3-axis translation stage with the cylindrical lens mount situated inside the Helmholtz coil mount.

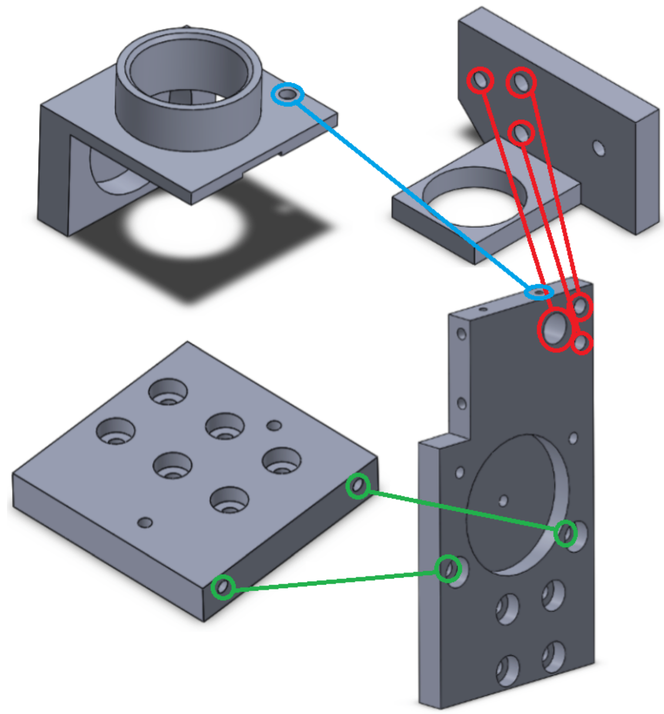

Figure 2.10: The final imaging mount design broken down into the major 4 pieces. Not pictured here are the triangle brackets used to add rigidity to the top plate for the 3-axis translation stage.

2.3 Implementation

After the design was completed we had the Physics Machine Shop build each of the mount's pieces out of aluminum. We then glued the cube and imaging optic onto their respective parts before assembling the rest of the optics. Before introducing the imaging system into the experiment, we decided to characterize the assembly outside of the experiment as a final check. To do so, we repeated the procedure described in [21] that was used to characterize the resolution before the mount had been made. We illuminated a 1μm pinhole, which was placed inside of a glass cell, with a collimated 780nm beam and then using the imaging lens to create a magnified image which was captured on a CCD camera. This setup mimics that of our experiment where the 1μm pinhole is meant to act like a point source, meaning the image we retrieve should characterize the impulse response function. After aligning the system so that it had a magnification of approximately 25 times, we took the image shown in Figure 2.11b. Taking the FWHM of this airy pattern and converting this to an imaging resolution we find that the imaging resolution is ~ 2μm which is slightly larger than what was found previously but is still within the range of usable resolutions. For reference, we are planning on imaging a lattice with lattice spacing of $1-2\mu$m and this sets the scale for our desired resolution. It is also important to note that the image has no noticeable astigmatisms.

After these tests, we moved forward with adding the imaging system to the experiment. In order to fit the mount into place, we had to removed the back plate and reattach it after the lens was inside the Helmholtz coil mount as the mount was too tall otherwise. Once the back plate was attached we bolted the mount onto a 3-axis translation stage. At this point it is important to note that our height measurements were off due to the lack

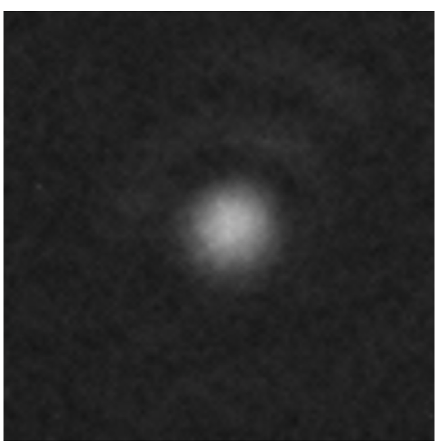

(a)

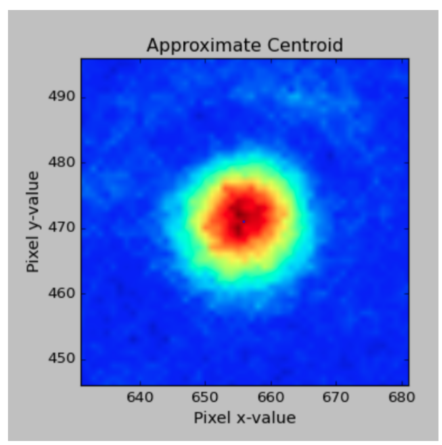

(b)

Figure 2.11: Images of a 1μm pinhole illuminated with 780nm light at ~ 25 times magnification. Here each pixel is $6.8\mu\text{m}\times6.8\mu$m. Note the fringes which match the Airy pattern as expected. The alignment of the light through the pinhole is responsible for the asymmetry of the Airy pattern's intensity.

of the bottom z-compensation coil. What this meant was that the entire system sits lower than originally planned for meaning we can only achieve a magnification of ~ 4 times with the current lens. Since the system is already designed with the maximum amount of space between the lens and the dichroic, one cannot fix this problem without buying a new imaging optic. As this magnification is still better than that of our current imaging system, we elected to proceed without purchasing a new optic. Unfortunately, the fact that the imaging optic will not be placed approximately a focal length away from the trap will present some complications for lattices that will be discussed later.

Since the holes for mounting to the 3-axis translation stage were made for

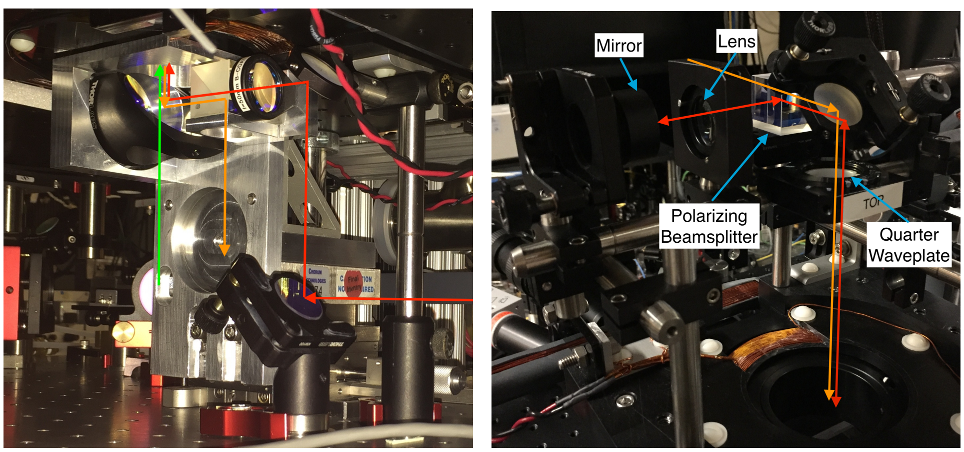

(a) (b)

Figure 2.12: Images of the imaging system installed in the experiment. The lower side of the experiment is shown in (a) with the apparatus from Figure 2.9. The green path will be that of a vertical lattice once installed, the red path is for the MOT beam and the orange path is the imaging path. Note that the second 2" mirror along the lattice path has not yet been installed as we currently don't have a lattice. There is also no camera in place yet for the imaging path as that will be installed once the ODT alignment is completed. The 50mm lens along the MOT path is used to counteract the effect of the imaging optic on the MOT beam as together they form a 1-to-1 telescope.

a specific height we had to mill them out into slots to secure the mount. After which, we used the triangle brackets to attach the back plate onto the mount before securing it to the translation stage. Despite these modifications, the entire mount is very rigid. One can account for the lack of magnification with a second imaging optic, although this will further decrease the resolution of the system. A picture of the imaging mount and routing optics is shown in Figure 2.12a.

Upon testing the components, we realized that the dichroic has a strong birefringence which meant we had to modify the system further by placing the quarter waveplate between the cell and the dichroic so that the light that was reflected from the dichroic was either “S” or “P” polarized.

This can complicate the implementation of a vertical lattice as the waveplate most likely won’t function properly at those wavelengths but this was the most obvious and immediate fix. Ideally, we would want the waveplate to not act as a waveplate at the lattice wavelength. To secure the waveplate we made a simple device, shown in Figure 2.13, that would allow one to lock the waveplate in place while allowing a degree of tuneability. For MOT

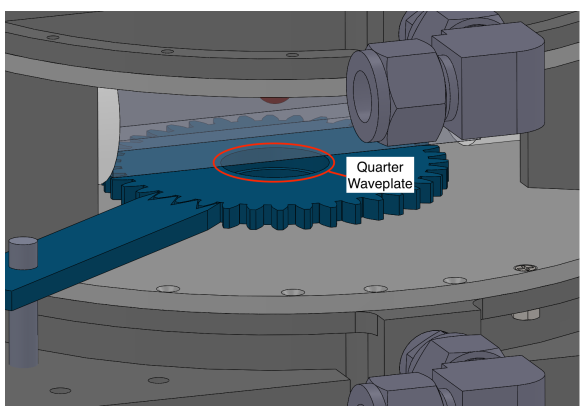

Figure 2.13: A SolidWorks drawing of the simple quarter waveplate mount for the imaging system. The appendage on the left allows one to lock the quarter waveplate’s angle. The quarter waveplate sits inside the gear on a small circular ledge made by a thin ring attached below the gear. The waveplate is then glued to this ledge for stability. This entire mount is thin enough to slide into place between cell and Helmholtz coil mount.

functionality, the quarter waveplate's angle does not need to be tuned extremely precisely and therefore the teeth on the gear were designed to give an angular precision of 10°.

We also found that the vertical MOT beam no longer looked quite Gaussian after passing through the imaging system as can be seen in Figure 2.14. It seemed as though this was due to the large size of the MOT beam (~ 1" in diameter) relative to the 1" mirrors. Since the periscope shown in Figure 2.12a uses 1" mirrors, their vertical size is only $1/\sqrt{2}$" ≈ 0.71" which means the vertical MOT beam is clipped. One should note that this is also an issue for the other MOT beams as they use similar optics, however it seems as though the imaging system amplifies this problem. As a consequence of this aberration, it is no longer possible to fully collimate the beam. We tried to find the source of the aberration but none of the optical components seemed to be individually responsible but rather the entire assembly. This could be due to the large beam diameter relative to many of the optics, resulting in a non-negligible portion of the beam being lost. This effect is usually unnoticeable when dealing with single optics but if at multiple points along the beam path a portion of the beam is lost, this can result in a non-Gaussian beam.

After we added the imaging system into the experiment, we built the top section pictured in Figure 2.12b to retro-reflect the MOT beam as we

Figure 2.14: An image of the vertical MOT beam taken in the far-field after having passed through the vertical imaging system. Note the ring pattern with the obvious intensity spike towards the edge. Various attempts to reshape the beam produced other odd patterns but none could transform it into a Gaussian pattern.

had decided to introduce the vertical MOT beam from the bottom of the apparatus. The mirror for retro-reflection is placed inside of a threaded tube to give fine control on its placement. This allows us to control the divergence of the retro-reflected beam since it couldn't be fully collimated.

2.3.1 Effect of the Vertical Imaging Optics on the Atom Loading Performance of the MOT

After reoptimizing the setup we achieved the MOT atom loading performance shown in Figure 2.15b. While this is worse than without the imaging system, it is important to note that the ODT saturates above $\sim 30 \times 10^6$ atoms in the MOT. As such, we have deemed this change in MOT performance to be unfortunate but within reason and have not sought to further increase our loading rate or steady state atom number.

At this time, the dipole trap is being set up and so there are no images from the vertical imaging system with which we can analyze its final performance. However, we did perform some preliminary tests of the system to see if its performance was in accordance with my data from my undergraduate thesis [21]. This characterization is described at length in Michael Kinach's report and we found that the imaging system had a resolution of approximately 1.9μm at 671nm. While this is larger than what was initially predicted, a more thorough test should be done with atoms in a dipole trap. An image taken with the system using a 1μm pinhole is shown in Figure 2.11a suggests that there are no major astigmatisms.

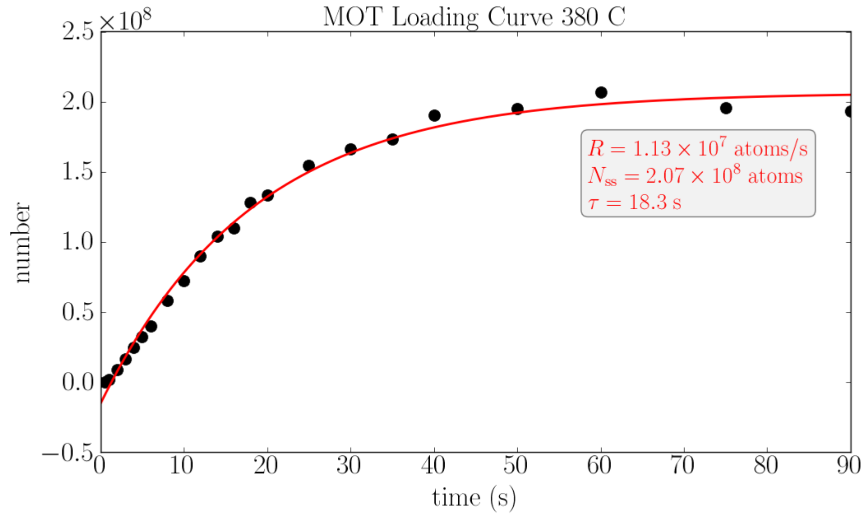

(a)

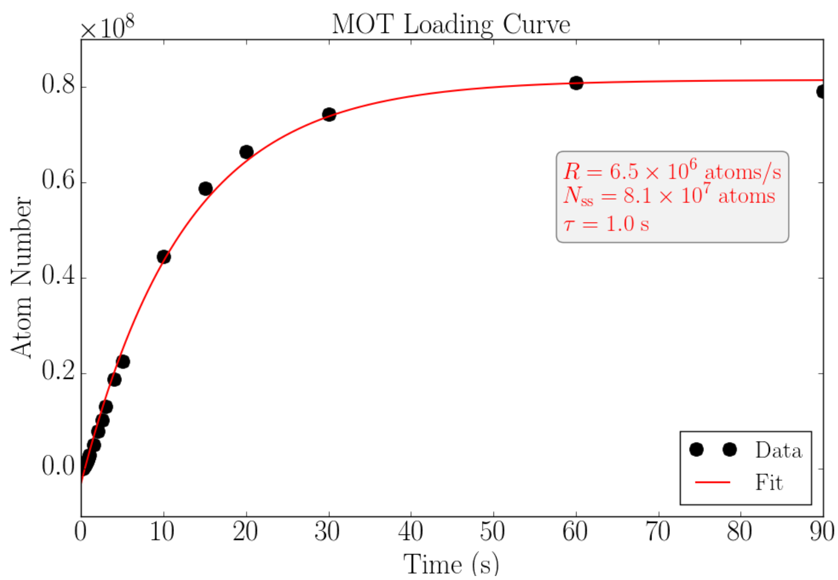

(b)

Figure 2.15: A comparison of MOT loading curves at 380°C. The loading curve before the imaging system was added is shown in (a) while the curve after it was added is shown in (b). One should note that for the data with the imaging system, the Zeeman slowing beam had been telescoped up by a factor of approximately 2 which inevitably changes the intensity profile along the slowing axis. This can in part be responsible for the difference between the two loading curves.

Chapter 3

The Dilating Lattice

Without the use of sophisticated optical arrangements, like those in [23–26], most imaging systems can achieve a resolution comparable to the 2μm resolution we achieved with the vertical imaging system. This can be a sufficient resolution for time-of-flight experiments, spectroscopy and even atomic interferometry. Certain experiments require the ability to detect single atoms. For a certain class of experiments one can use a micro-channel plate (MCP) based detection scheme to achieve such resolutions, although this method is specific to metastable atoms and can't be used to get information *in situ* [27].

A recent development is the creation of the so-called quantum gas microscope which is a high fidelity imaging system capable of resolving separations between atoms less than a micron in size [23–26]. These high resolution imaging systems require a pinning lattice to hold the atoms in place during the image. Imaging atoms in a lattice allows one to have well defined positions for atoms which we showed in Section 2.1.1 can increase the SNR by 3 orders of magnitude. So far, these quantum gas microscopes are both extremely expensive but also of limited use for imaging a quantum gas that is not confined by a lattice. This specificity may narrow down the types of experiments one can perform with a given apparatus.

An alternative to both of these schemes is to expand the spacing between the particles so that their physical separation is greater than the resolution of the imaging system. This second perspective has lead to the invention of the dilating lattice. Simply put, these lattices are created with a mechanism for dynamically varying the lattice spacing. The is commonly achieved by changing the separation of two parallel beams before they are focused by a lens to then create a lattice as depicted in Figure 3.1. While there are various schemes for doing so, we have modified the design used by Mark Raizen's group [28]. This modification and proof-of-principle is detailed in this chapter.

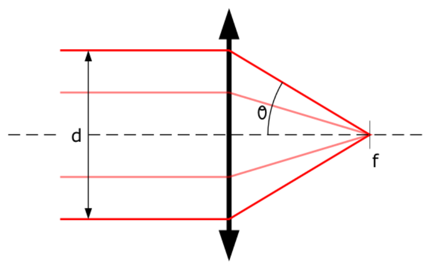

Figure 3.1: A depiction of the mechanism responsible for the interference creating the lattice. If two beams intersect at some oblique angle, they can generate an interference pattern with a periodicity dependent on their angle of intersection. A lens will take two beams and intersect them at some point on the focal plane, which means the angle of intersection is dependent on the separation of the two beams d.

3.1 Theory

An optical lattice is generated by the interference of at least two light waves. Usually, this takes the form of two laser beams intersecting one another at a desired location. So, to start, we refer to the standard wave equation

$$\nabla^2 u(\vec{x},t) - \frac{1}{c^2}\frac{\partial^2 u(\vec{x},t)}{\partial t^2} = 0 \tag{3.1}$$

where $u(\vec{x},t)$ is the wavefunction and $c = \frac{c_0}{n}$ is the reduced speed of the wave in the medium. Since this is a linear equation, we know that obeys the laws of superposition, which is the key to understanding interference. Since we will be assuming our light is monochromatic, it makes sense to write our wavefunction as the real part of some complex wavefunction $U(t,\vec{x})$. In particular, we usually write

$$U(\vec{x},t) = U_0(\vec{x})e^{i\varphi(\vec{x})}e^{i2\pi\nu t} \tag{3.2}$$

where $\varphi(\vec{x})$ is the phase of the wave, ν is the frequency and $U_0(\vec{x})$ is some spatially varying amplitude. We often define the complex amplitude to be $U(\vec{x}) = U_0(\vec{x})e^{i\phi(\vec{x})}$ and therefore we can then define the optical intensity $I\left|(\vec{x})\right| = \left|U(\vec{x})\right|^2$.

Now, these $U(\vec{x},t)$ also obey the wave equation and hence they also obey the superposition principle. Therefore, the intensity of a wave composed of two waves with complex amplitudes $U_1(\vec{x})$ and $U_2(\vec{x})$ is given by

$$\begin{aligned} I &= \left|U_1\right|^2 + \left|U_2\right|^2 + U_1^* U_2 + U_1 U_2^*, \\ &= I_1 + I_2 + 2\sqrt{I_1 I_2}\cos\varphi, \end{aligned} \tag{3.3}$$

where $\varphi = \varphi_1 - \varphi_2$ is the phase difference between the two waves.

3.1.1 Plane Wave Interference

To start with a more simple analysis of our system, we examine two plane waves intersecting at some angle 2θ. If we assume both plane waves are polarized along the axis perpendicular to their plane of intersection, we can drop the polarization of the waves and simply write

$$U_1 = \sqrt{I_1}e^{-ik(\cos\theta z + \sin\theta x)}, \qquad U_2 = \sqrt{I_2}e^{-ik(\cos\theta z - \sin\theta x)}. \tag{3.4}$$

Using Equation 3.3, we find then that that

$$\begin{aligned} I &= I_1 + I_2 + \sqrt{I_1 I_2}e^{i2kx\sin\theta} + \sqrt{I_1 I_2}e^{-i2kx\sin\theta}, \\ &= I_1 + I_2 + 2\sqrt{I_1 I_2}\cos(2kx\sin\theta), \end{aligned} \tag{3.5}$$

which in turn implies that $\varphi = 2kx\sin\theta$. Hence, the interference has a periodicity of $\pi/k\sin\theta$ or, in terms of wavelength, $\lambda/2\sin\theta$. If we refer again to Figure 3.1, if this is generated by a lens, we obtain

$$\sin\theta = \frac{1}{\sqrt{1 + (2f/d)^2}} \tag{3.6}$$

where f is the focal length and d is the separation of the beams. We can then see that the lattice periodicity is given by

$$a = \frac{\lambda}{2}\sqrt{1 + \left(\frac{2f}{d}\right)^2} \tag{3.7}$$

which means that if one were to generate a lattice using two 532nm beams, using a lens with a diameter of 50mm and a focal length of 40mm, we could obtain a lattice spacing as small as 500nm. In the limit where $d/2 << f$ we find that $a \approx \lambda f/d$ which means one could theoretically achieve an arbitrarily large lattice spacing. One needs to consider that, as a consequence of the divergence of the lattice spacing as $d \to 0$, a small change in d will result in a large change in the lattice spacing. Therefore, the stability of the lattice spacing is becomes strongly correlated with the stability of the optical components. For instance, vibrations in mirror mounts can cause small angular changes which turn into non-negligible changes in d and therefore large changes in a. Therefore, one will reach a point where the stability of the lattice spacing is predicated on the stability of the optical path.

3.1.2 Gaussian Beam Interference

When dealing with lasers, light is usually in the form of Gaussian beams and so we will hereby take into account the higher order effects the come with this more complicated situation. Recall that a Gaussian beam has a complex amplitude given by

$$U(\vec{r}) = U_0 \frac{W_0}{W(z)} e^{-\frac{x^2+y^2}{W(z)^2}} e^{-i\left(kz + k\frac{x^2+y^2}{2R(z)} - \zeta(z)\right)}. \tag{3.8}$$

If we use this expression in Equation 3.3, we can analytically determine the intensity field. This was done in [29] and assuming the beams are angled in the xz-plane, as shown in Figure 3.2, we can write that the phase difference as

$$\varphi = -k(z_1 - z_2) + \zeta(z_1) - \zeta(z_2) - \frac{k}{2}\left[\frac{x_1^2 + y_1^2}{R(z_1)} - \frac{x_2^2 + y_2^2}{R(z_2)}\right] \tag{3.9}$$

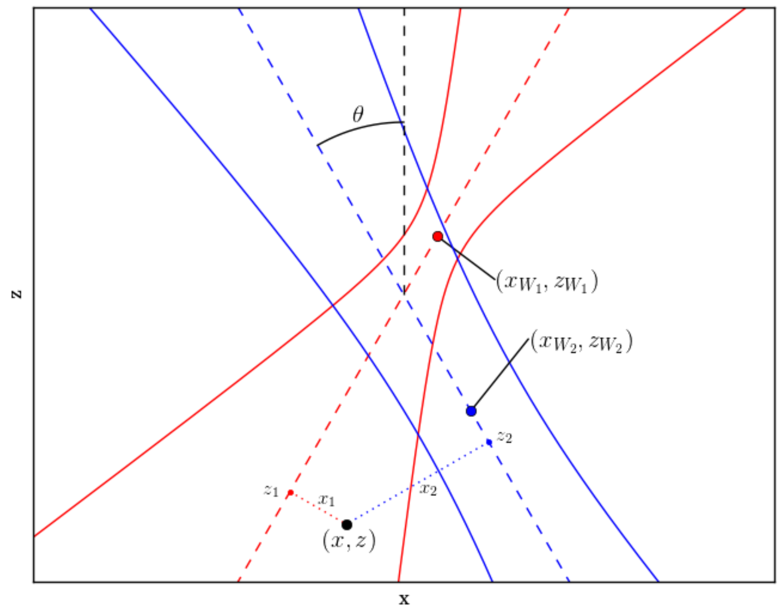

Figure 3.2: A depiction of the scenario described in Section 3.1.2. Here we can see the relationship between the lab coordinate system (x, z) and the beam coordinate systems (x_1, z_1) and (x_2, z_2). Note the lab frame positions of the beam waists shown as (x_{W_1}, z_{W_1}) and (x_{W_2}, z_{W_2}) in the figure. Lastly, the angle θ bisects the angle between the two beams defining a natural way to orient the lab frame's coordinate system.

where

$$
\begin{aligned}
x_1 &= x\cos\theta + z\sin\theta, \\
x_2 &= x\cos\theta - z\sin\theta, \\
z_1 &= -(x - x_{W_1})\sin\theta + (z - z_{W_1})\cos\theta, \\
z_2 &= (x - x_{W_2})\sin\theta + (z - z_{W_2})\cos\theta,
\end{aligned} \tag{3.10}
$$

and the subscript W_i denotes the location of beam i's waist in space. This leads to a the lattice spacing being expressed as

$$
a = \frac{\lambda}{2\sin\theta}\left[1 + \frac{\left(\frac{x_1 z_1}{z_1^2 + z_{0_1}^2} - \frac{x_2 z_2}{z_2^2 + z_{0_2}^2}\right)}{2\tan\theta - \left(\frac{x_1 z_1}{z_1^2 + z_{0_1}^2} - \frac{x_2 z_2}{z_2^2 + z_{0_2}^2}\right)}\right] \tag{3.11}
$$

where $z_{0_i} = \frac{\pi W_{0_i}^2}{\lambda}$. Note that the first term is the same as we found for plane waves, and it is the second term that is the deviation from this simple behaviour. If both beams have the same waist size and position along the $z-$axis, Equation 3.11 simplifies to

$$
a = \frac{\lambda}{2\sin\theta}\left(1 + \frac{1}{\phi - 1}\right) \tag{3.12}
$$

where

$$
\phi = \frac{2}{z_1}\frac{z_1^2 + z_0^2}{x_1 - x_2}\tan\theta. \tag{3.13}
$$

This geometric factor ϕ now encodes all of the specifics of the Gaussian beams. One should note that the case when $\theta \to 0$ means that the lattice spacing scales twice as fast as in the plane wave case. Likewise if $\theta \sim 45°$ then the points where z_1,z_0,x_1 and x_2 all be comparable also have a lattice space which is twice the plane wave case. As such, we can see quite a dramatic shift away from the simple plane wave case by including this geometric factor.

An example of what the intensity pattern would look like for the case of two equivalent beams is shown in Figure 3.3. These simulations will let us more accurately determine the lattice spacing as we change the angular separation of the incoming lattice beams.

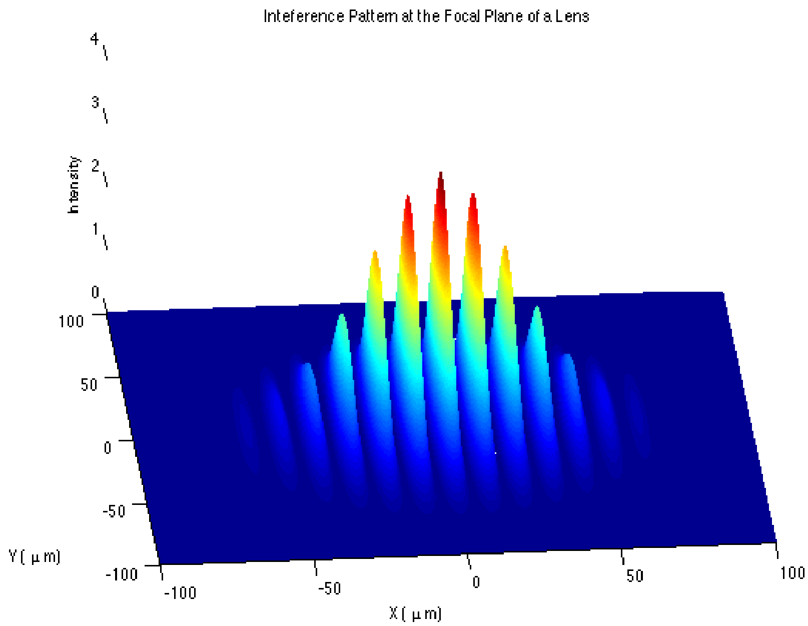

Figure 3.3: The prediction for the intensity pattern created by interfering two identical Gaussian beams propagating relative to each other by 3°. The beams are at a wavelength of 532nm, with beam waists of 50μm at the interference plane.

3.2 Design

Given our understanding of interference as a phenomena created by differences in phase, the two main issues the dilating lattice design one must address is how one will actually dilate the lattice as well as how the phase, from the path difference between the beams, will be kept constant. This second aspect is in some ways secondary, however it is crucial to the actual implementation of the system as a variation in the difference in path length will cause the lattice to shift.

We originally aimed to implement the design shown in Figure 3.4. It is a modification to a Michelson interferometer, whereby the lens $L2$ acts to flip the vertical position of the horizontal beam. As one can see, we shift the beam splitting cube labelled $B1$ along the vertical direction to change the vertical beam's horizontal placement. This is the mechanism by which we would change the separation of the beams before they are focused, and subsequently interfered, by the lens $L1$.

Unfortunately, the usage of $L1$ means that one arm of the interferometer has a changing path length with respect to the other as the angled path between $L2$ and $M2$ varies as the beams are separated. One could conceivably account for this with some mechanism to shift $M1$ accordingly but this solution seemed inelegant. We wished for a system that had a constant difference in path length without the need for some active stabilization.

To that end, we adopted the design in [28]. One can easily see that the relative path lengths of the two arms are always the same, within the uncer-

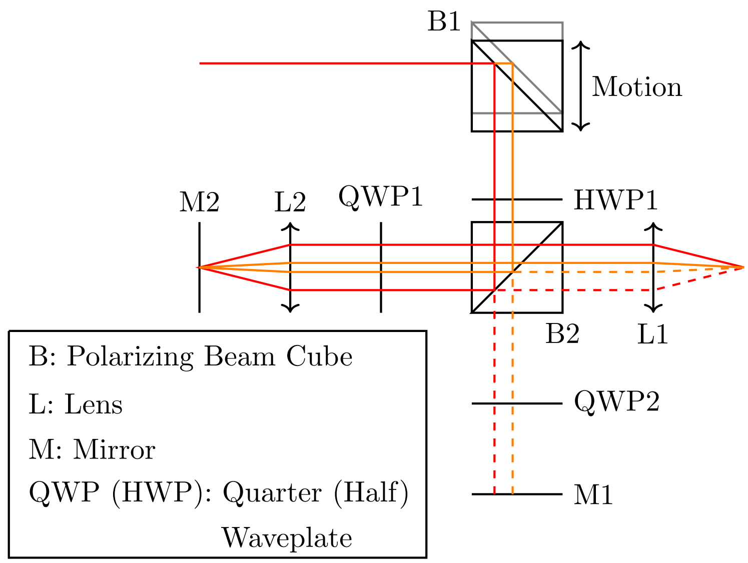

Figure 3.4: The original design for our dilating lattice. By translating the $B1$ polarizing beam splitting cube, we change the horizontal position of the vertical beam. We then use the $L2$ lens, along with the $M2$ mirror, to reflect one of the split horizontal beams about the lens' axis. This creates two parallel beams with a tuneable separation which we can then interfere using the $L1$ lens.

tainty due to components. One would need to implement a compensation path to initially adjust the path lengths of the two arms so that the beams have the same divergence and size at $L1$, in Figure 3.5, since we are assuming we will use Gaussian beams. Unfortunately for this design, to achieve a large lattice periodicity, one must place the beams very close to one another. In this design, how close they can get is constrained by the quality of the beam cubes at their edges.

It is at this point we modified this design to account for this problem. The final design is depicted in Figure 3.6. The modification is done so that the two beams are recombined in one beam cube. This is beneficial because we can then move the beams arbitrarily close to one another, generating a lattice with as large a periodicity as one would like. It limits how small a lattice one can achieve, however increasing the size of the beam cube B3 can be used to decrease this restriction. It also maintains the constant relative path length property and as such, one can just stabilize the mirror $M2$ to

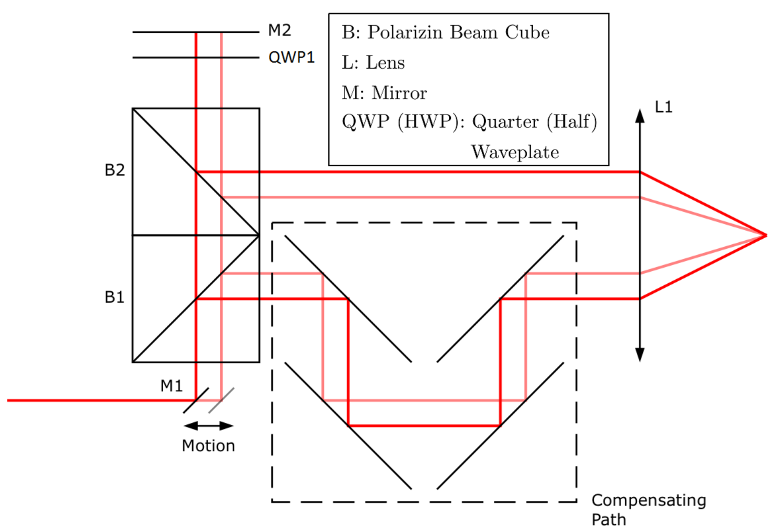

Figure 3.5: An alternative design from [28]. This uses a horizontal (or vertical) translation of $M1$ to determine the location at which the beam is split on $B1$. The symmetry of this design creates a second parallel beam and we implement a compensating path to adjust the relative path length.

account for vibrations or other changes in the system.

Using this design, we can reasonably achieve lattice spacings varying from 0.8μm to 50μm using 532nm light and a lens with a numerical aperture of 0.55. To then determine the minimum sizes of the components we can rearrange Equation 3.7 to get

$$d = \sqrt{\frac{(2f)^2}{1-\left(\frac{2a}{\lambda}\right)^2}} \tag{3.14}$$

which means $B3$, $P1$ and $L1$ must be at least 28.2mm in diameter.

To be able to take advantage of such a large lattice spacing we would require the beam diameters be large at the focal plane. We therefore analyze the effect of the initial waist position on the beam size around the focal plane after the lens $L1$. Recall that the Gaussian beam is characterized by its q parameter and for an optical system defined by its $ABCD$ matrix, we have

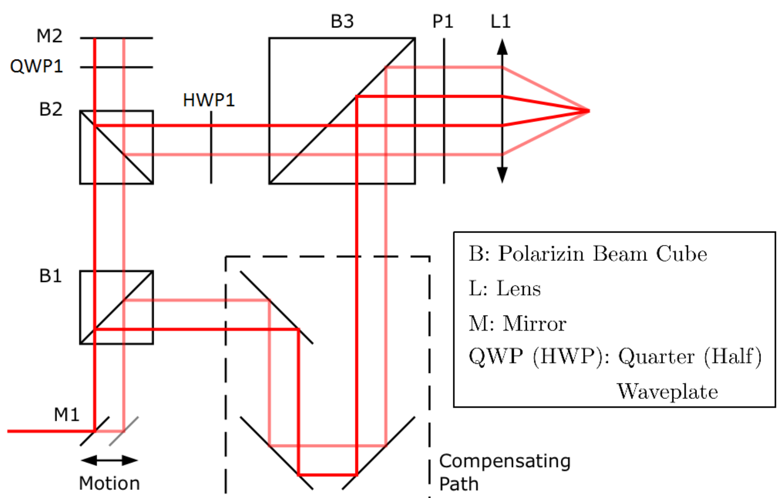

Figure 3.6: A modified version of the design presented in [28]. This design recombines the split beams in a third beam cube $B3$ to allow for arbitrarily small beam separation.

that

$$q_2 = \frac{Aq_1 + B}{Cq_1 + D} \qquad\qquad \frac{1}{q_2} = \frac{C + D\frac{1}{q_1}}{A + B\frac{1}{q_1}}. \tag{3.15}$$

Now, if we first consider an incident beam on the lens that is then modified by its transmission through the lens and then the free space after it until the focal plane, the $ABCD$ matrix would be

$$\begin{pmatrix} A & B \\ C & D \end{pmatrix} = \begin{pmatrix} 1 & f \\ 0 & 1 \end{pmatrix} \begin{pmatrix} 1 & 0 \\ -\frac{1}{f} & 1 \end{pmatrix} = \begin{pmatrix} 0 & f \\ -\frac{1}{f} & 1 \end{pmatrix}. \tag{3.16}$$

Hence, we can see that

$$\frac{1}{q_2(\tilde{z})} = \frac{1}{R_2(\tilde{z})} - i\frac{\lambda}{\pi W_2(\tilde{z})^2} \tag{3.17}$$

$$= \frac{1}{f} - \frac{q_1}{f^2}$$

$$= \frac{f - z}{f^2} - i\frac{z_0}{f^2} \tag{3.18}$$

where $\tilde{\tilde{z}}$ is the distance between the focused beam's waist and the focal plane of the lens. If we then take the imaginary part of Equation 3.17 and compare it to the imaginary part of Equation 3.18, we find that

$$\frac{z_0}{f^2} = \frac{\lambda}{\pi W_2(\tilde{z})^2} \implies W_2(\tilde{z}) = \frac{\lambda}{\pi}\frac{f}{W_0}. \tag{3.19}$$

This tells us that the beam size at the focal plane is independent of the initial beam's waist location. Therefore, if we want $W(\tilde{z}) \geq 50\mu$m, then this requires that $W_0 \lesssim 135\mu$m. As the lattice will exist in some spatial region around the focal plane of the imaging lens, we need to understand the trap shape for different input Gaussian beam parameters. Figure 3.7 summarizes the complicated interplay between the initial beam waist, the initial waist location and the final beam size.

In Figure 3.7d, we can see that the beam size at the image plane (which is 4cm in this simulation) is independent of the initial beam's waist location as we just derived. From Figure 3.7b, we can also see that the most collimated beam occurs when the initial beam waist's location is at the focal length of the lens (which is again 4cm in this simulation). Other beam waist locations give rise to beam which have a larger variation in beam size along the propagation axis (here labelled as the imaging plane location). This makes sense as the lens then acts to collimate the beam. Needless to say, these parameters will be adjusted in the final setup to make sure that both beams have a beam size of at least 50μm at the focal plane of the lens.

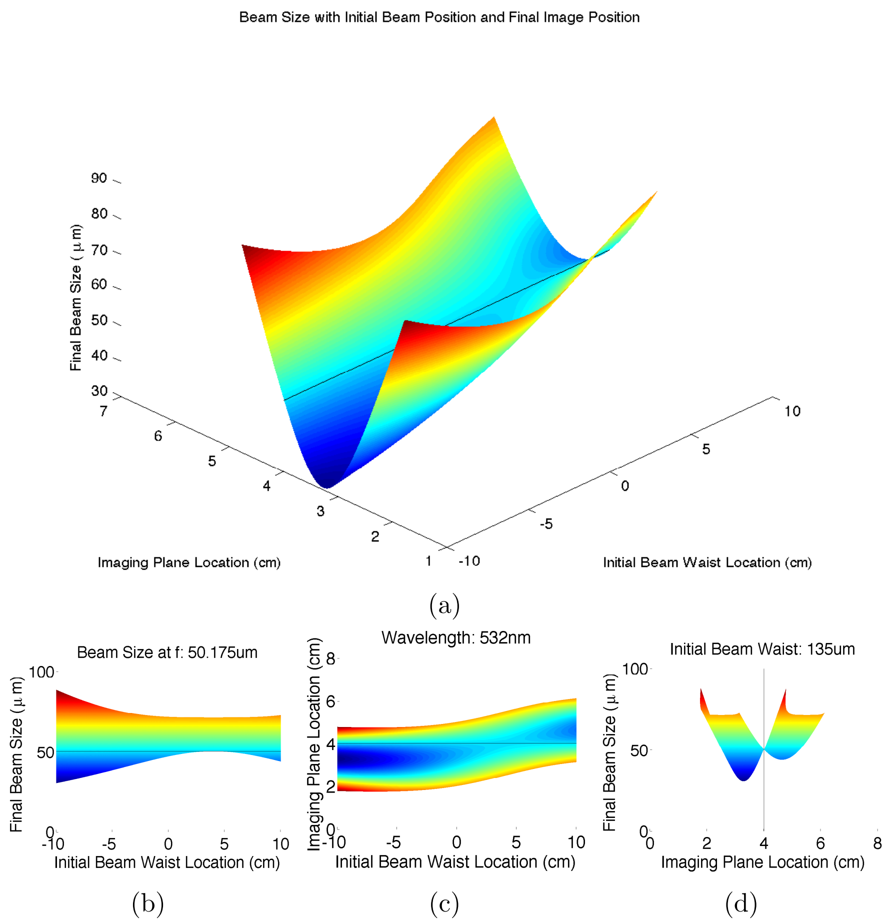

Figure 3.7: A depiction of the Gaussian beam size at different position along the propagation axis (labelled here as the imaging plane location) for different initial beam waist sizes and locations. For these simulations, the focal length of the lens is 40mm. The black line marks the focal plane of the lens. The entire surface relating the three parameters is shown in (a) while (b),(c), and (d) are projections along each axis to make reading the plot easier. A cross section of (a) taken parallel to the plane of (d) is the Gaussian beam size as a function of z. As such, different cross sections relate what the different output Gaussian beams look like for different initial waist locations. The projection of the surface in (b) gives you an idea of the collimation of the output beams for different initial waist locations. Note that the beam is tightly focused if the beam waist is located on the opposite side of the lens compared to the beam was (i.e. at -10cm) while at an initial beam waist location of 5cm the beam is significantly more collimated. The projection in (c) shows that the focus of the Gaussian beam changes as the initial beam waist locations changes as we would anticipate.

3.3 Implementation

To test the design depicted in Figure 3.6, we built a test system shown in Figure 3.8 using 780nm light due to its abundance in our lab. We used a simple translational stage for adjusting the beam separation which we could then detect on the camera. To determine accurately the relative beam alignments, we set up a pair of flip mirrors to allow us to switch between a

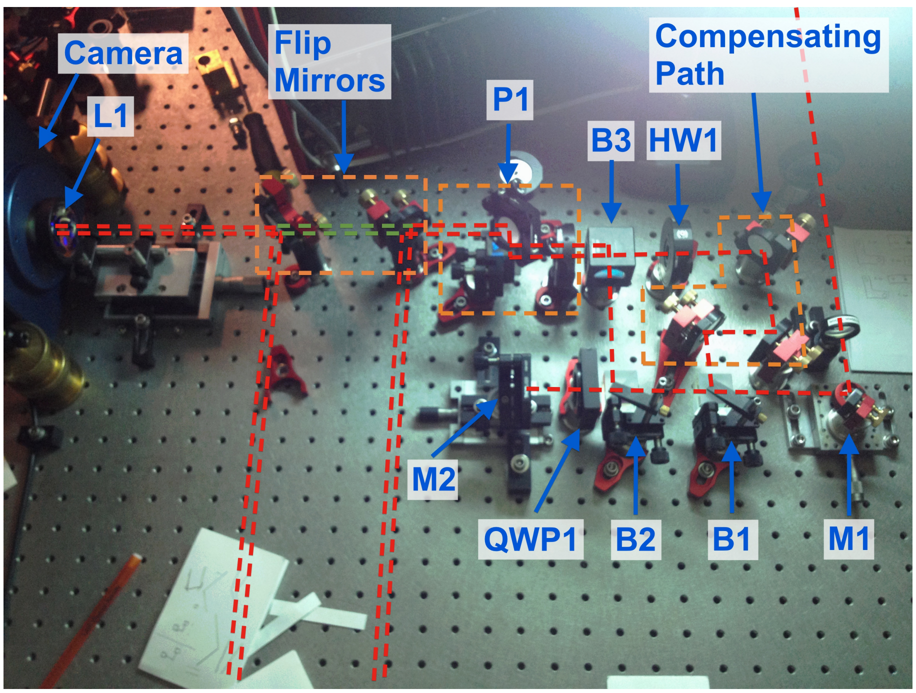

Figure 3.8: The setup pictured here is a realization of the design shown in Figure 3.6 with the main difference being the addition of the flip mirrors. This pair of mirrors allows us to alternate between the short green path and long red path which travels out of the frame. Not pictured here are two mirrors that connect the long beam path at the bottom of the picture. Due to the higher height of the camera, we needed to include a periscope P1 to raise the beam heights to match that of the camera. A diagram of the periscope is shown in Figure 3.9. The unlabelled optics before M1 are for shaping the beam and preparing its initial polarization.

short and long path before striking the camera.

This allowed us to quickly determine if the beams were parallel by detecting their locations on the camera and looking for changes in their relative positions. A sample image showing the two beams on the camera is shown in Figure 3.10. By iterating between the two paths, we could achieve a relative shift of ~ 0.5mm over an extra 1m of propagation (which equates to a 0.03° angular difference).

Using the lens labelled L1 in Figure 3.8, we interfered the two beams and imaged the resulting intensity pattern. We then tuned the translation stage and took pictures for various translations. A selection of those pictures is shown in Figure 3.11.

As a sanity check we unlocked the 780nm lasers and saw the interference disappear. This is due to the laser's frequency drifting on a timescale much faster than the exposure time of the camera and thus any interference pattern is blurred out.

Once we locked the laser, we saw that we recovered the interference pattern we expected to see. At this point, we translated $M1$ and saw that the interference pattern's periodicity varied accordingly. This is shown in

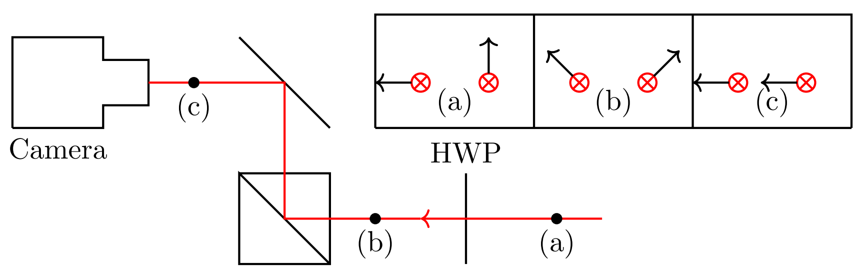

Figure 3.9: The diagram of the periscope P1 from Figure 3.8. We used a polarizing beam cube as the bottom mirror to project the two lattices beams' polarizations onto the same axis. At point (a) the polarizations of the two incoming lattice beams are orthogonal as is shown in the inset. We rotate the polarizations so that they're 45° to the conventional "S" and "P" polarizations that way when the two beam reflect from the cube, their polarizations are parallel. If we did not include this cube, the lattice beams would not interfere.

Figure 3.11. The rotation of the interference pattern is also expected because the system isn't perfectly aligned. This is caused by the difference in beam height's as they hit the lens as shown in Figure 3.12. This can serve as a test of the positional alignment of the two beams relative to the lens. One might find this rotating behaviour undesirable but it should be noted that it can be eliminated by using a cylindrical lens, although if two orthogonal lattices were to be generated by a single lens this solution wouldn't work.

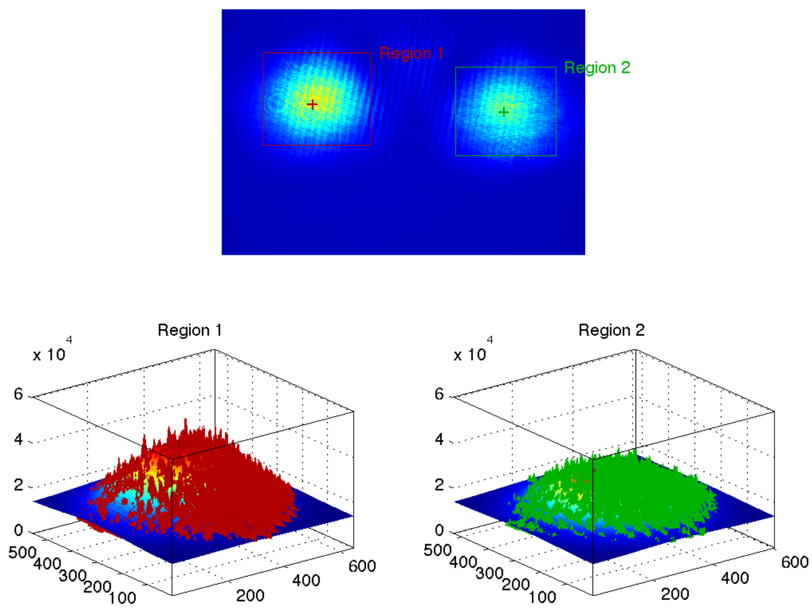

Figure 3.10: A sample image showing the two dilating lattice beams on the camera and the output of our peak finding algorithm. The algorithm takes the picture shown at the top and determines the center position of the two beam. It does so by fitting a Gaussian intensity distribution to each region of interest (as outlined in the top picture). This allows us to accurately determine the beams' positions.

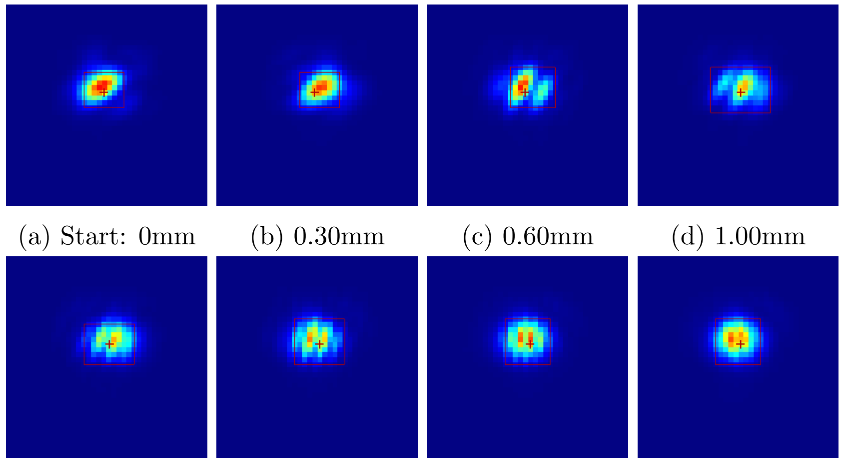

(a) Start: 0mm (b) 0.30mm (c) 0.60mm (d) 1.00mm

(e) 1.30mm (f) 1.70mm (g) 2.00mm (h) 2.50mm

Figure 3.11: A demonstration that the system performs as expected. Without calibrating the entire system absolute positions are meaningless so we have labelled each picture by the amount the translation stage was moved. We can see that the periodicity changes as we vary the $M1$ mirror's placement. Note the orientation of the lattice rotating as the beam separation changes due to the imperfect alignment of the system.

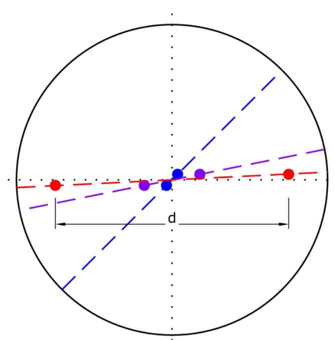

Figure 3.12: A cartoon demonstrating the effect of imperfect alignment on the interference axis. Here the pairs of coloured dots represent the positions of the pairs of dilating lattice beams. The dashed lines that intersect these pairs of points denote the axis along which the pairs of beams will interfere to form the interference pattern. Notice how, if the beams are misaligned, the axis along which interference occurs changes as the beams get closer.

3.4 Beam Translation Options

In the above work we manually adjusted the beam's position before it was split on the first beam cube B1. We wish to be able to vary the separation of the beams on the timescale of a typical experiment, which is ~ 1s, in a repeatable fashion. To this end, we investigated a couple of different options for translating the beam.

3.4.1 Linear Actuators

The first linear actuator we considered attaching to a translation stage was a T-NA Micro Linear Actuator. As linear motion seemed like the most obvious choice and we had this actuator in the lab we decided to test it first. Using an Arduino UNO as a controller, we implemented a hall sensor on the actuator to keep track of the position of the actuator. After calibrating the sensor and controller, we found that, although the rate of motion is fast enough for our purposes, there is a lot of jitter associated with the actuator. Since the stability of the mirror in motion will translate to the stability of the beams (and hence the dipole trapping mechanism itself), the presence of jitter in the motion is thought to cause heating in the trap.

We also tried the Newport CMA Linear Actuator. Instead of the Arduino, we could control the position and velocity via the Newport Universal Motion Controller. This device allows us to carefully set the velocity of the stepper motor and displays on the screen the current location. Also, we may choose to connect this to any computer and control it via a software, which will most likely be our choice for controlling the actuator. Furthermore, in comparison to the T-NA Micro Linear Actuator, the Newport actuator is noticeably far more stable - there is no jittery motion associated with the actuation. While having all of the qualities stated above, we found this actuator to be extremely slow. The CMA Linear Actuator has a maximum velocity of 0.4mm/s, which means it will take 50s to travel the entire length of the beam splitter cubes, which have a side length of 2cm. 50s is longer than the expected trapping time for the experiments the lab plans to conduct, so this rate of motion will not work for the dilating lattice. After doing some research on these actuators, there seems to be no way of increasing the velocity to above 0.4mm/s. If we were to utilize this linear actuator, then we would have to use it in some other, clever way, instead of simply linearly translating the mirror in the setup.

We decided to investigate using a linear actuator to rotate a mirror about some axis. To mimic the behaviour of the beam under the linear translation of a beam, we then place a lens after the rotating mirror to have the beam come out parallel to our standard horizontal axis for each angle of rotation. The rotation was implemented roughly by removing the knob associated with the horizontal angling in a standard mirror mount, and replacing it with the linear actuator as shown in Figure 3.13. The tip of the actuator will penetrate through the mount and press against the mirror side where the knob usually sits, allowing us to angle the mirror with the actuator instead of manually turning the knob.

Next, we placed the rotating mirror between the two lenses of our telescope for collimating the beam, so that the second lens behaves as part of

Figure 3.13: The rotating setup with the Newport CMA Linear Actuator. As we can see, the knob associated with the horizontal motion is removed and the actuator tip is inserted to achieve the rotating motion.

the telescope while making the beams parallel as well. For our test, we focused the beam with the initial lens such that the waist occurred at the mirror, then placed the second lens with a focal length of 10cm after the rotating mirror. We quickly realized that the careful positioning of this lens was very important, since the focus needs to be right at the beam's axis of rotation in order for this setup to behave properly. This sensitivity was further amplified by the dilating lattice's sensitivity to alignment. If the lens was either too close or too far from the mirror, the output beam from the lens is not going to be parallel for the entire length the mirror scans. To carefully adjust and achieve the focal length to coincide with the axis of rotation, we placed this lens on a translation stage. After many iterations, the positioned lens was able to send the beams straight out of the plane of the lens as required over a distance of over one meter, thus verifying that the rotating mirror and lens combination is able to achieve what a single translation stage can do at directing the beam.

The most significant benefit of this alternative design is the fact that a relatively slow actuator can be transformed into a fast, linear beam displacement, since we are adjusting a small angle over a rather long distance; however, along with some benefits, issues that cannot be ignored arise here which were not present in the original design. In order to get a reasonably large range of motion, one needs to either angle the mirror a substantial amount or the beam needs to propagate for a larger distance. The larger angle requires the actuator to act for longer, decreasing the benefit for slow actuators. The long distance can also have an impact on the stability of the system. Another major flaw is the sensitivity of the lens' position as even a small adjustment can destroy the parallel beam output.

Lastly, we note that with the standard mirror mounts, the point at which the beam reflects from the mirror changes as the rotation takes place. This is due to the mirror mount's pivot point being offset from the mirror's center as shown in Figure 3.14. This is problematic as the distance to the lens will shift as the rotation takes place, resulting in the beams which are not parallel. Although the beams were relatively parallel over about a meter distance, we saw this as an issue. To solve this problem, we switched to a gimbal mount. Using this mount, we were able to achieve the mirror's axis of rotation to be at the centre of the mirror - this is necessary in order to keep the focus of the beam to be fixed such that the outgoing beam's are parallel with respect to one another.

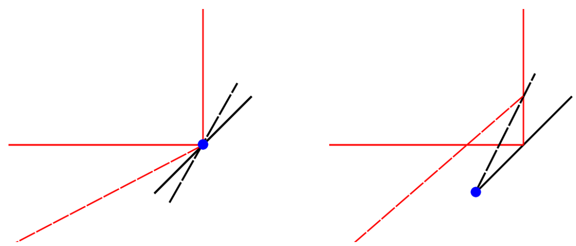

(a) (b)

Figure 3.14: (a) The ideal rotation of a mirror achieved using a gimbal mount. The blue dot is the axis of rotation. (b) Non-ideal rotation of a mirror using a standard mirror mount. The blue dot is the axis of rotation.

3.4.2 Rotation via an AOM

Instead of physically rotating a mirror, the idea was to use the first order beam from an AOM to translate the beam in a similar setup to the rotating mirror method. By changing the AOM's drive frequency, we effectively change the angle at which the beam is reflected, hence allowing the AOM to behave the way our rotating mirror did. A benefit to the setup is the fact that we could eliminate the physical translation of an actuator in favour of changing an RF frequency input. This gives us a significant advantage as the AOM is significantly faster than any physical actuator and we can smoothly sweep the frequency, eliminating any jitter in the motion.

Unfortunately, we found that due to the small angular displacement, the change in position was about 1cm over a path length of approximately 1m. Considering that we are aiming for the beam to translate a total of 2cm, this was a significant flaw. One could in principle use a telescope to magnify this angular displacement but this added complexity was not ideal. However, if one were to consider a lattice which would have a lattice spacing varying from 1μm to 5μm, this would be more feasible. In this case, if we solve for d in Equation 3.3 we find that

$$d = \frac{2f}{\sqrt{(\frac{2a}{\lambda})^2 - 1}} \tag{3.20}$$

If we then take δd to be the difference in space between the beams for the two lattice spacings, then $\delta d/2$ is the distance a single beam must move to be able to change from a separation of 1μm to 5μm. Recalling that we have been considering our a 532nm wavelength beam with a lens with a focal length f=40mm, we can substitute in a_1=1μm and a_2=5μm into Equation 3.20 to find that $\frac{\Delta d}{2}$=8.9mm. Since we have already verified that the AOM can displace the beam about 1cm if it is about a meter away, the AOM method may be viable for this type of small separation.

3.4.3 Zaber's T-NA Micro Linear Actuator

After we investigated all of these options, it seemed clear that the linear actuator was the best option if we could find a motor with enough range and speed. We found that Zaber's T-NA Micro Linear Actuator satisfied all of our criteria as it is able to travel 25mm at a maximum velocity of 8mm/s. This linear actuator will be able to output up to a 50N thrust, so it will be able to handle any of the translation stages with which we decide to pair it. The quoted repeatability is less than 1μm which corresponds to a very small shot-to-shot variation of the beam separations and thus angles (and therefore also lattice periodicities).

3.5 Design of the Monolithic Container

While the proof-of-principle was built on an optical table, one needs to make sure the entire apparatus is interferometrically stabilized to reduced jitter in the lattice spacing and phase. As such I hereby outline a design for a monolithic container for the lattice optics.

The simplicity of the optics affords one to make a relatively portable and compact system which outputs two beams with variable spacing which can then be directed towards the location one wishes to generate a lattice. In this way, one can decouple the more complicated aspect of the design from the rest of an experiment's optical system. Since alignment of this system seems to be more crucial than most optical systems in ultracold systems, having the option of removing a box containing all of the elements so that one can realign in a more suitable environment is a significant advantage. Over the course of several weeks we noticed no passive drift in the dilating lattice system. We did so by periodically taking images of the two beams as shown in Figure 3.10 and analyzed their positions and found no discernable drift within the uncertainty of our fitting routine which was on the order of 300μm. This suggests that so long as one makes a rigid container, the optics will remain aligned for an extended period of time.

The design, shown in Figure 3.15, mimics our realization of Figure 3.6 in a more compact manor with the optics designed for this application. To reduce drift, we have made pedestals, upon which the cubes would sit instead of adjustable mounts. Some of the components must be on adjustable mounts so that we can achieve the very accurate parallel beam orientation that we previously achieved on the optics table. To further increase the portability of the design, we have made it take a fiber for an input so that one can easily add it to a system with minimal alignment. At the opposite end, where the two parallel beams will be exiting the container, we will have to slits for the beam to potentially be able to leave from - this is so that we can use one of the exits for alignment purposes while the other one will be for the actual dilating lattice. As we lose half of the light by projecting the two beams' polarizations onto the same axis, we have designed it to have two output slits - one for alignment purposes and the other for the actual dilating lattice.

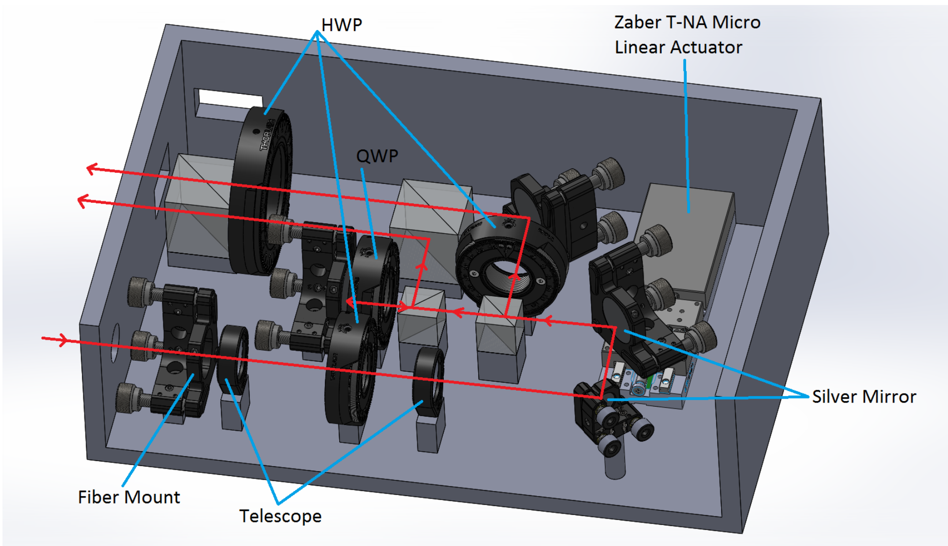

Figure 3.15: A Solidworks drawing of the container. Note that the unlabelled mirrors are normal mirrors for the lattice wavelength and all of the cubes are polarizing beam cubes. The reason we need two silver mirrors is because the half waveplate on the input will tune the polarization of the incoming light to be an even split between "S" and "P" polarized. With normal dielectric mirrors, if the polarization isn't either just "S" or "P" then the reflected polarization is not guaranteed to be linear. One should also note that the input to the box is designed to be a fiber, fed through the hole in the bottom left corner and mounted in the fiber mount. This makes the system much more portable. Also not drawn, there is a second rejection port which has the orthogonal polarization pair to the drawn output beams.

Chapter 4

Methods for Determining Collisional Decoherence Rates

4.1 Motivation

Another area of interest within our group is studying many-body physics using ^{6}Li and Rb atoms. Within this broad area of interest, we became interesting in using Feshbach resonances to tune collisional decoherence rates of superposition states after discussing our experiment with the authors of [30]. Decoherence is an important mechanism by which a system can transition between quantum and classical realms, and it is therefore of fundamental interest to physicists. Due to this effect, it is often times a limiting factor for quantum experiments and collisional dechorence is often times uncontrollable due to its stochastic nature. However, this proposal would give researchers a simple method of suppressing decoherence using Feshbach resonances.

To measure the decoherence rate, we had set about using microwaves from an RF coil to induce Rabi oscillations between hyperfine states of ^{6}Li. We would then look for decoherence in the oscillations which would manifest itself as a decrease in the amplitude of the oscillations. We could then measure this decrease in amplitude as a function of interaction strength. This proposal will be discussed in more detail in Section 4.3.

4.2 Theory

4.2.1 Rabi Oscillations

Rabi oscillations come from the coupling of at least two states via some time varying electromagnetic field. To see how those oscillations come about, we start by considering the system shown in Figure 4.1. Here we have a light field that is detuned from the $|e\rangle \to |g\rangle$ transition by δ (i.e. $\omega = \omega_0 + \delta$). In the electric dipole approximation, we assume that the variation of the electric field over the dipole is negligible and we can therefore write

$$\boldsymbol{E}(t) \approx \boldsymbol{E}_0 \cos(\omega t). \tag{4.1}$$

Therefore, the coupling term in the Hamiltonian can be written as

$$H_{\text{int}} = 2\Omega \cos(\omega t) \left(|e\rangle \langle g| + |g\rangle \langle e| \right) \tag{4.2}$$

where

$$\Omega = -\frac{\boldsymbol{E}_0}{2} \cdot \langle g| \boldsymbol{d} |e\rangle \tag{4.3}$$

is called the Rabi frequency for reasons that will become apparent soon. The Hamiltonian takes this simple form because the diagonal terms are zero due to the parity of the dipole operator and we can choose the phase of

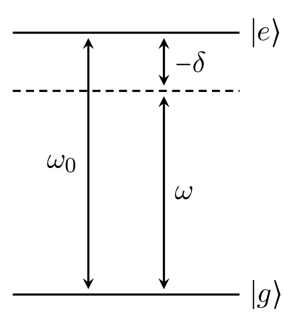

Figure 4.1: A standard 2-level system with a light field of frequency ω. Here we note that the energy separation (in units of frequency) between the $|1\rangle$ and $|2\rangle$ state is ω_0 and the light field is detuned from this transition by δ.

the dipole operator such that the off-diagonal matrix elements are real. Let us now consider some general unperturbed state $|\Psi(t)\rangle = c_g |g\rangle + c_e e^{-i\omega_0 t} |e\rangle$ where the time dependence comes from the unperturbed atomic Hamiltonian $H_{\text{atom}} = \hbar\omega_0 |e\rangle \langle e|$.

Note that although the time dependence of each state's projection is normally included in the coefficients c_g and c_e, I have elected to write it as a separate term for clarity in this short aside. If we then consider the expectation value of the interaction Hamiltonian by this general state one finds that this gives

$$\begin{aligned}\langle\Psi(t)| H_{\text{int}} |\Psi(t)\rangle &= \Omega \left(e^{i\omega t} + e^{-i\omega t}\right) \left(c_e^* c_g e^{i\omega_0 t} + c_g^* c_e e^{-i\omega_0 t}\right) \\ &= \Omega \left[c_e^* c_g e^{i(\omega+\omega_0)t} + c_g^* c_e e^{i(\omega-\omega_0)t} + c_e^* c_g e^{-i(\omega-\omega_0)t} + c_g^* c_e e^{-i(\omega+\omega_0)t}\right]\end{aligned} \tag{4.4}$$

If we then focus on systems where $|\omega - \omega_0| = |\delta| << \omega + \omega_0$ then we can neglect the rapidly oscillating terms of the form $e^{\pm i(\omega_0+\omega)t}$ and focus on the slower frequency terms. This approximation is called the rotating wave approximation. As such, we can write our simplified Hamiltonian as

$$H_{\text{int}} \approx \frac{\hbar\Omega}{2} \left(e^{-i\omega t} |e\rangle \langle g| + e^{i\omega t} |g\rangle \langle e|\right) \tag{4.5}$$

We can now write the total Hamiltonian of Figure 4.1 as $H = H_{\text{atom}} + H_{\text{int}}$. If one now considers some state $|\Psi(t)\rangle = c_g(t) |g\rangle + c_e(t) |e\rangle$, taking the projections against $\langle g|$ and $\langle e|$ of the time dependent Schrödinger equation gives

$$i\partial_t c_g = \frac{\Omega}{2} c_e e^{i\omega t} \tag{4.6}$$

$$i\partial_t c_e = \frac{\Omega}{2} c_g e^{-i\omega t} + \omega_0 c_e. \tag{4.7}$$

A standard method for solving these sorts of equations is to switch to a rotating reference frame by defining $\tilde{c}_e = c_e e^{i\omega t}$, In this new rotating frame, these equations can be written as

$$i\partial_t c_g = \frac{\Omega}{2}\tilde{c}_e \tag{4.8}$$

$$i\partial_t \tilde{c}_e = \frac{\Omega}{2}c_g + (\omega_0 - \omega)\tilde{c}_e \tag{4.9}$$

or in matrix form as

$$i\hbar \begin{pmatrix} \tilde{c}_e \\ c_g \end{pmatrix} = \tilde{H} \begin{pmatrix} \tilde{c}_e \\ c_g \end{pmatrix} \tag{4.10}$$

where

$$\tilde{H} = \hbar \begin{pmatrix} -\delta & \Omega/2 \\ \Omega/2 & 0 \end{pmatrix}. \tag{4.11}$$

To find the eigenstates of this system of equations one simply needs to diagonalize this rotating frame Hamiltonian, the results of which are

$$|E_\pm\rangle = \frac{(\delta \pm \tilde{\Omega})\,|g\rangle + \Omega\,|e\rangle}{\sqrt{2\tilde{\Omega}(\tilde{\Omega} \pm \delta)}} \tag{4.12}$$

where the eigenenergies are

$$E_\pm = -\frac{\hbar}{2}\left(\delta \mp \tilde{\Omega}\right). \tag{4.13}$$

and $\tilde{\Omega} = \sqrt{\delta^2 + \Omega^2}$ is called the generalized Rabi frequency. The energy of the coupled states is shown in Figure 4.2 which demonstrates the avoided crossing characteristic of coupled states.

To illustrate why Ω is called the Rabi frequency, let us consider the case where $\delta = 0$. In this case, our eigenstates simplify to

$$|E_\pm\rangle = \frac{\pm|g\rangle + |e\rangle}{\sqrt{2}} \tag{4.14}$$

with $E_\pm = \pm\frac{\hbar}{2}\Omega^2$. Then if we started with an atom in the lower state, one can write

$$|\Psi(t=0)\rangle = |e\rangle = \frac{|E_+\rangle - |E_-\rangle}{\sqrt{2}} \tag{4.15}$$

and therefore, the population in the excited state after some time t is

$$\begin{aligned} P_e(t) = |\langle e|\ \Psi(t)\rangle|^2 &= \left|\langle e| \left(\frac{e^{-i\frac{\Omega}{2}t}|E_+\rangle - e^{i\frac{\Omega}{2}t}|E_-\rangle}{\sqrt{2}} \right)\right|^2 \\ &= \left|-i\sin\left(\frac{\Omega}{2}t\right)\right|^2 \\ &= \frac{1-\cos\Omega t}{2}. \end{aligned} \tag{4.16}$$

Therefore, we see that Ω is the frequency with which the population oscillates between the two states. This phenomenon is called Rabi flopping and

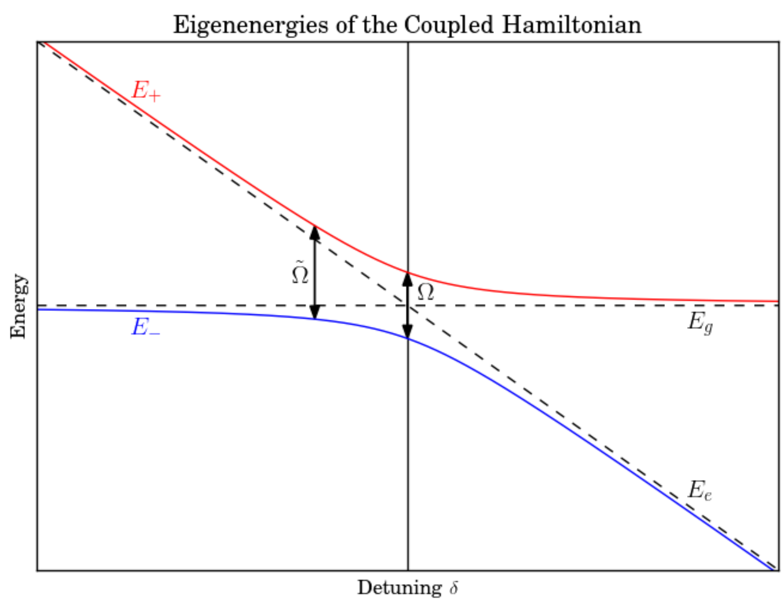

Figure 4.2: A plot of the eigenenergies of the rotating frame Hamiltonian written in Equation 4.13. Note that as the magnitude of the detuning increases, the system increasingly acts like an uncoupled system as one would expect.

one can show that for $\delta \neq 0$, the population in the excited state (assuming $|\Psi(t=0)\rangle = |g\rangle$) is given by

$$P_e(t) = \left(\frac{\Omega}{\tilde{\Omega}}\right)^2 \frac{1-\cos\tilde{\Omega}t}{2}. \tag{4.17}$$

We can see that if the light is off resonance, the amplitude of the oscillations is not unity meaning the state of the atom is never fully in the excited state, as shown in Figure 4.3.

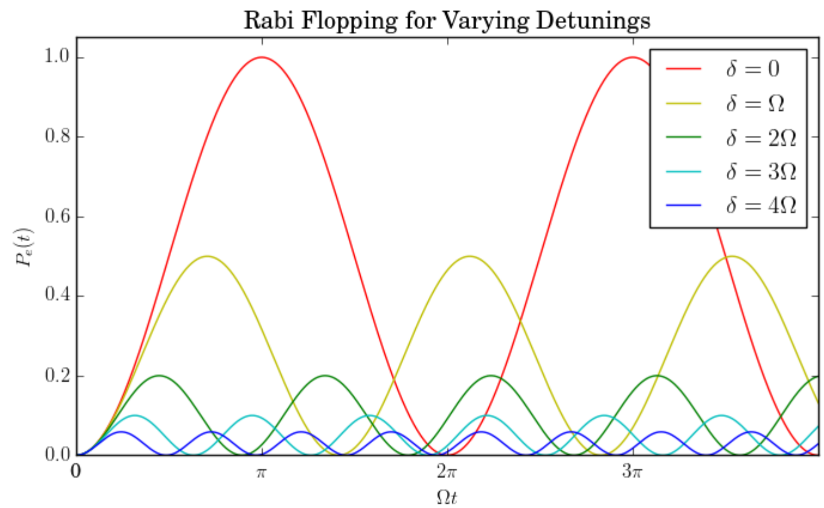

Figure 4.3: A comparison of the effect the detuning has on Rabi flopping. Note that this scaling behaviour matches our intuition as a far-from-resonant laser should cause almost zero coupling between levels in the system.

4.2.2 Adiabatic Passage

A useful consequence of the avoided cross shown in Figure 4.2 is the ability to transfer atoms between the $|g\rangle$ and $|e\rangle$ by simply tuning the frequency. For instance, if the atom is in state $|g\rangle$ and one were to sweep the frequency of the light across the resonance slow enough so that it adiabatically follows the coupled curves, then when the light is once again far detuned, the atom will be in the $|e\rangle$ state. This is called adiabatic passage and requires that the sweep rate is slow enough for the atom to stay in an eigenstate of the coupled Hamiltonian.

One then naturally asks how slow the sweep rate has to be for the population to be transferred with almost unit probability. This is what is called the Landau-Zener problem [31, 32] and it has been shown that the probability of the atom to not transfer to the desired state is given by

$$P_{\text{lost}} = e^{-\frac{\pi}{2}\frac{\Omega^2}{|\partial_t \delta|}} \tag{4.18}$$

where $|\partial_t \delta|$ is the sweep rate. This assumes that you start and finish your sweep far-detuned, otherwise you would project your initial or final state onto the eigenstates of the system causing an extra decrease in efficiency. To have close to unit probability of transfer, one wants $|\partial_t \delta| << \Omega^2$.

One of the reasons this phenomena is so important is due to the robustness of this technique. For Rabi flopping, one is very sensitive to the energy splitting between the $|g\rangle$ and $|e\rangle$ states as this corresponds to a change in the detuning. For instance, one can imagine shining an on-resonant laser ($\delta = 0$) on some trapped atoms in the $|g\rangle$ state. If one were to then leave this laser on for a time $t = \pi/\Omega$ then all of the atoms should be transferred to the $|e\rangle$ state. However, as is the case in many experiments, if there were to exist an inhomogeneous magnetic field in the region of one's trapped atoms then the energy splitting can vary as a function of location due to a differential Zeeman shift. This would cause the generalized Rabi frequency to vary with position, quickly causing the different atoms in the trap to oscillate out of phase with one another, meaning that after the laser is turned off the population will no longer be uniformly populating the $|e\rangle$ state.

Since one is just tuning the frequency across the resonance, shifts in the resonance position make little difference to the efficiency of adiabatic transfer. This makes it much more robust to a large number of experimental disturbances.

4.3 The Effect of Collisional Decoherence on Rabi Oscillations

As previously mentioned, we had thought to use the sensitivity of Rabi flopping to our advantage when trying to measure collisional decoherence. The experiment we had in mind started with ^{6}Li atoms in a dipole trap with the population split evenly between the $|1\rangle$ and $|2\rangle$ states (as defined in Figure 2.3b). At magnetic field of at least 100G, these states are split by approximately 76MHz. We can then use an RF coil to drive Rabi oscillations in the atoms between the $|2\rangle$ and $|3\rangle$ states which have a splitting of 158MHz. We can then tune the collisional cross section of the $|1\rangle$ and $|3\rangle$ state atoms

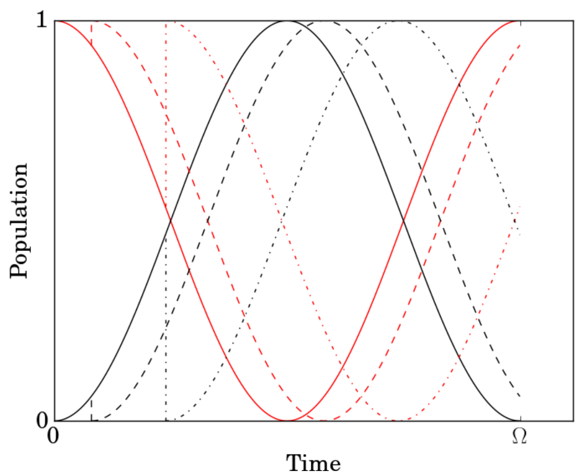

Figure 4.4: A depiction of the time evolution of an atom's state's components. Here the red (black) solid line is the population in the $|2\rangle$ ($|3\rangle$) state without any collisions. As soon as a collision happens, the atom's state is projected onto purely the $|2\rangle$ state as represented by the discontinuity between the solid and dashed line. Now any of the atoms, either in the solid or dashed time evolving paths, can have a collision projecting them into the $|2\rangle$ again, this time drawn as the dotted line. One can then see that quickly these different possible evolutions of state become out of phase with one another. This will then lead to the decrease in the amplitude of Rabi oscillations averaged over the entire ensemble.

around a Feshbach resonance and examine the effect this has on the rate at which dephasing occurs in the Rabi oscillations. This is because the inelastic scattering of $|1\rangle$ and $|3\rangle$ state atoms produce two $|2\rangle$ atoms which carry away approximately 30μK of energy. As such, one can picture the atom superposition state changing because of this loss as shown in Figure 4.4. Each time this atom experiences a collision with a $|1\rangle$ state atom, the $|2\rangle$ and $|3\rangle$ are set to 1 and 0 respectively due to the collisions products. Since the occurence of this collision will happen at different times for different atoms, one will see that the resulting dephasing of the Rabi oscillations will scale with the collisional cross section. Thus we should be able to tune the decoherence time of the Rabi flops with the Feshbach resonance.

Before proceeding with our experimental results, we should note that a recent paper from Dr. Rudolf Grimm's group [33] measures a similar effect except, instead of using three hyperfine states of a single species, they use a superposition of two hyperfine states in one atom interacting and decohering due to collisions with a second atom of a different species. Their experimental method uses a RF pulse sequence to interferometrically measure the decoherence rate.

4.3.1 Experimental Results

Our first objective was to see if we could see Rabi flopping between the $|1\rangle$ and $|2\rangle$ states as their collisional rate should be small. To do so, we shone high-field imaging light (i.e. imaging light which has its frequency tuned to correct for the shift in transition frequency due to high magnetic fields) on the ^{6}Li atoms in the trap to empty one of the two hyperfine states before turning on our RF coil for some time. We would then image either of the states after varying the duration that the RF coil had been on to reconstruct the population in each of the states as a function of time. Unfortunately, even with a 5W amplifier to increase the RF power, and therefore the Rabi frequency, we were unable to see any evidence for coherent Rabi flopping. We simply saw what looked like a random percentage of the total population in each state. We also tried the transitions between the $|1\rangle$ and $|3\rangle$ states and the $|2\rangle$ and $|3\rangle$ states but were met with the same noise-like data. This noise would even persist on the shortest time between subsequent commands for our experiment (6μs) which seemed to suggest some other environmental factor was causing transitions.

To test this, we repeated the exact same procedure but didn't actually turn the RF coil on. In this case, we saw the populations in each state remain fixed, suggesting that the noise was somehow due to the RF field we were exposing the atoms to. We then considered the scenario where our Rabi frequency was significantly larger than we had anticipated. In this case, the noise could be some sort of aliasing of rapid Rabi oscillations. To characterize our coil, and the Rabi frequency it produces, we swept the RF frequency across the resonance to adiabatically transfer atoms between

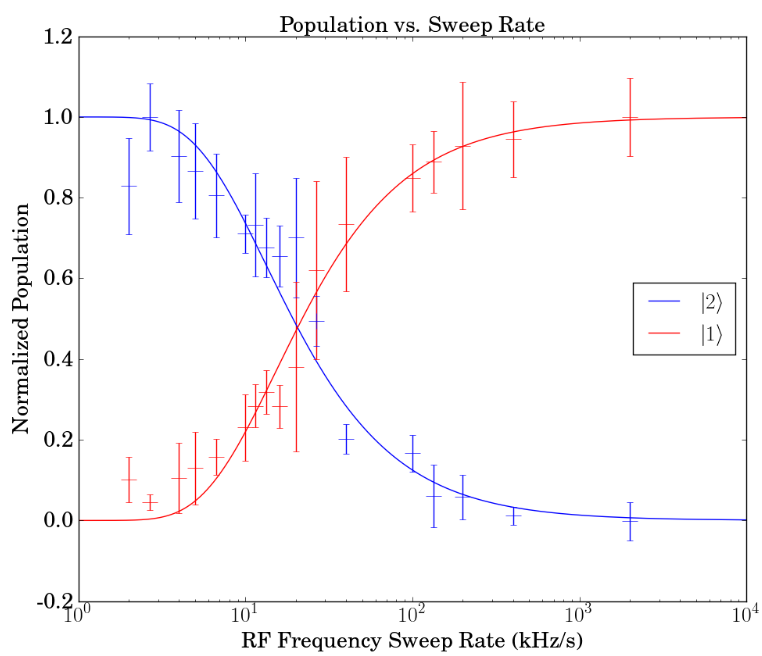

Figure 4.5: The efficiency of the transfer between the $|1\rangle$ and $|2\rangle$ states for various sweep rates. We then fit this data using Equation 4.18 to determine the Rabi frequency which is approximately 100Hz.

states. We did this for various sweep rates and this data is shown in Figure 4.5. From fitting this data, we determined that the Rabi frequency of our coil on the $|1\rangle \rightarrow |2\rangle$ to be on the order of 100Hz which was much too low to cause the transitions we were seeing.

At this point the experiment started becoming more dedicated to spectroscopic endeavours required for performing STIRAP, resulting in this research being postponed. We did however purchase the 30W Mini-Circuits LZY-22+ amplifier and build a better RF coil to increase the achievable Rabi frequencies for when we return to this research direction.

Chapter 5

Conclusion

The tools we have developed over the course of this thesis have been built to not only push forward towards our goal of STIRAP and the formation of ultracold molecules, but also to enhance the possibility of investigating many-body phenomena in a dual species experiment.

The vertical imaging system can be used for both ^{6}Li and *Rb* provided one has two cameras placed at different locations to account for the chromatic aberration. This increase in the SNR by a factor of 2, due to the new vertical orientation of our imaging system, will allow one to detect the small number of molecules created via STIRAP. The higher resolution and magnification will also make it possible to image the cloud of atoms and detect some spatial structure within the cloud. Currently, the entirety of the atomic cloud takes up approximately 20 pixels on our camera meaning one can only make gross measurements of our system without releasing and letting the atoms expand. In order to take advantage of these new opportunities though, one must finish the imaging system by introducing the camera into the system and focusing it on our dipole trap. As soon as the dipole trap is aligned and optimized, this will be one of the first things our lab does.

A longer goal is to realize the dilating lattice, prototyped here, along the vertical axis of the experiment. This will allow us to load all of the atoms into one or two lattice sites, when the lattice is expanded, before decreasing the lattice spacing and compressing our atoms. One could then investigate 2D physics in these pancake potentials on top of the more standard lattice physics experiments to which the dilating lattice would provide access. Most of the work presented on this lattice was discussed using 532nm light but we are currently considering using 1064nm light from our dipole trap lasers to form the lattice. In order to realize this design however, one needs to work out how to stabilize the lattice apparatus interferometrically in order to minimize changes in the lattice's position and spacing.

Finally, the work towards observing Rabi flopping between hyperfine states of ^{6}Li remains unfinished. After some encouraging results, the focus of the experimental work shifted to making molecules. In preparation for the resumption of this research, a new RF coil has been made and we have bought a 30W Mini-Circuits LZY-22+ amplifier. This coil has been designed to better impedance match our RF input, increasing the radiated power and hence our Rabi frequencies. The amplifier was purchased with the same motivation and together they should be able to generate Rabi frequencies on the order of 100kHz which is 4 orders of magnitude larger than is currently accessible. This then means one will be able to probe shorter timescales as the oscillations will happen faster, giving one insight into the origin of our observed noise. Once this noise is identified and eliminated, one will have all of the tools necessary to make investigate the effect Feshbach resonances have on collisional decoherence rates.

Together, these three tools and techniques lay the foundation for our research in many-body quantum effects. The lattice will act both as a trap and tuning parameter, the Rabi oscillations due to the applied RF radiation will act as both a parameter and probe while the imaging apparatus is essential for the lattice and data acquisition. One of the motivating examples of this many-body research is the ability to simulate a Kondo Hamiltonian using the heavy Rb atoms pinned in a lattice immersed in a trapped gas of ^{6}Li atoms. It has been shown that this system is analogous to electrons moving in a metal [6] and therefore one can experimentally probe Kondo physics using cold atoms. This and other such experiments will now be available due to the work discussed in this thesis.

Bibliography

[1] W. Bowden. An experimental apparatus for the laser cooling of lithium and rubidium. Master's thesis, UBC, 2014.

[2] W. Gunton. Photoassociation and feshbach resonance studies in ultracold gases of ^{6}li and rb atoms, 2016.

[3] H. Müller, A. Peters, and S. Chu. A precision measurement of the gravitational redshift by the interference of matter waves. *Nature*, 463:926–929, February 2010.

[4] D. DeMille, S. B. Cahn, D. Murphree, D. A. Rahmlow, and M. G. Kozlov. Using molecules to measure nuclear spin-dependent parity violation. *Phys. Rev. Lett.*, 100:023003, Jan 2008.

[5] Johannes Kofler, Mandip Singh, Maximilian Ebner, Michael Keller, Mateusz Kotyrba, and Anton Zeilinger. Einstein-podolsky-rosen correlations from colliding bose-einstein condensates. *Phys. Rev. A*, 86:032115, Sep 2012.

[6] J. Bauer, C. Salomon, and E. Demler. Realizing a kondo-correlated state with ultracold atoms. *Phys. Rev. Lett.*, 111:215304, Nov 2013.

[7] Mariusz Semczuk, Xuan Li, Will Gunton, Magnus Haw, Nikesh S. Dattani, Julien Witz, Arthur K. Mills, David J. Jones, and Kirk W. Madison. High-resolution photoassociation spectroscopy of the ^{6}li$_2$ $1^3\Sigma_g^+$ state. *Phys. Rev. A*, 87:052505, May 2013.

[8] Will Gunton, Mariusz Semczuk, Nikesh S. Dattani, and Kirk W. Madison. High-resolution photoassociation spectroscopy of the ^{6}li$_2$ $a(1^1\Sigma_u^+)$ state. *Phys. Rev. A*, 88:062510, Dec 2013.

[9] A. Micheli, G. K. Brennen, and P. Zoller. A toolbox for lattice-spin models with polar molecules. *Nat Phys*, 2(5):341–347, May 2006.

[10] D. Jaksch and P. Zoller. The cold atom hubbard toolbox. *Annals of Physics*, 315(1):52 – 79, 2005. Special Issue.

[11] G. Igel-Mann, U. Wedig, P. Fuentealba, and H. Stoll. Ground-state properties of alkali dimers xy (x, y=li to cs). *The Journal of Chemical Physics*, 84(9), 1986.

[12] V. Tarnovsky, M. Bunimovicz, L. Vukovi, B. Stumpf, and B. Bederson. Measurements of the dc electric dipole polarizabilities of the alkali dimer molecules, homonuclear and heteronuclear. *The Journal of Chemical Physics*, 98(5), 1993.

[13] M. Aymar and O. Dulieu. Comment on calculation of accurate permanent dipole moments of the lowest +1,3 states of heteronuclear alkali dimers using extended basis sets [j. chem. phys.122, 204302 (2005)]. *The Journal of Chemical Physics*, 125(4), 2006.

[14] K.-K. Ni, S. Ospelkaus, M. H. G. de Miranda, A. Pe'er, B. Neyenhuis, J. J. Zirbel, S. Kotochigova, P. S. Julienne, D. S. Jin, and J. Ye. A high phase-space-density gas of polar molecules. *Science*, 322(5899):231–235, 2008.

[15] J. Deiglmayr, A. Grochola, M. Repp, K. Mörtlbauer, C. Glück, J. Lange, O. Dulieu, R. Wester, and M. Weidemüller. Formation of ultracold polar molecules in the rovibrational ground state. *Phys. Rev. Lett.*, 101:133004, Sep 2008.

[16] Y. C. Chen, C. E. Simien, S. Laha, P. Gupta, Y. N. Martinez, P. G. Mickelson, S. B. Nagel, and T. C. Killian. Electron screening and kinetic-energy oscillations in a strongly coupled plasma. *Phys. Rev. Lett.*, 93:265003, Dec 2004.

[17] Russell A. Hart, Pedro M. Duarte, Tsung-Lin Yang, Xinxing Liu, Thereza Paiva, Ehsan Khatami, Richard T. Scalettar, Nandini Trivedi,

David A. Huse, and Randall G. Hulet. Observation of antiferromagnetic correlations in the hubbard model with ultracold atoms. *Nature*, 519(7542):211–214, Mar 2015. Letter.

[18] William Bowden, Will Gunton, Mariusz Semczuk, Kahan Dare, and Kirk W. Madison. An adaptable dual species effusive source and zeeman slower design demonstrated with rb and li. *Review of Scientific Instruments*, 87(4), 2016.

[19] B. Deh, W. Gunton, B. G. Klappauf, Z. Li, M. Semczuk, J. Van Dongen, and K. W. Madison. Giant feshbach resonances in ^{6}Li-^{85}Rb mixtures. *Phys. Rev. A*, 82:020701, Aug 2010.

[20] Z. Li, S. Singh, T. V. Tscherbul, and K. W. Madison. Feshbach resonances in ultracold ^{85}Rb-^{87}Rb and ^{6}Li-^{87}Rb mixtures. *Phys. Rev. A*, 78:022710, Aug 2008.

[21] K. Dare. The design and characterization of a high-resolution imaging system, 2014.

[22] M. Semczuk. Photoassociation spectroscopy of a degenerate fermi gas of ^{6}li, 2015.

[23] Waseem S. Bakr, Jonathon I. Gillen, Amy Peng, Simon Folling, and Markus Greiner. A quantum gas microscope for detecting single atoms in a hubbard-regime optical lattice. *Nature*, 462(7269):74–77, Nov 2009.

[24] Jacob F. Sherson, Christof Weitenberg, Manuel Endres, Marc Cheneau, Immanuel Bloch, and Stefan Kuhr. Single-atom-resolved fluorescence imaging of an atomic mott insulator. *Nature*, 467(7311):68–72, Sep 2010.

[25] D. Jervis. A fermi gas microscope apparatus, 2014.

[26] Lawrence W. Cheuk, Matthew A. Nichols, Melih Okan, Thomas Gersdorf, Vinay V. Ramasesh, Waseem S. Bakr, Thomas Lompe, and Martin W. Zwierlein. Quantum-gas microscope for fermionic atoms. *Phys. Rev. Lett.*, 114:193001, May 2015.

[27] Michael Keller, Mateusz Kotyrba, Florian Leupold, Mandip Singh, Maximilian Ebner, and Anton Zeilinger. Bose-einstein condensate of metastable helium for quantum correlation experiments. *Phys. Rev. A*, 90:063607, Dec 2014.

[28] T. C. Li, H. Kelkar, D. Medellin, and M. G. Raizen. Real-time control of the periodicity of a standing wave: an optical accordion. *Opt. Express*, 16(8):5465–5470, Apr 2008.

[29] Paul C. Miles. Geometry of the fringe field formed in the intersection of two gaussian beams. *Appl. Opt.*, 35(30):5887–5895, Oct 1996.

[30] Jie Cui and Roman V. Krems. Collisional decoherence of superposition states in an ultracold gas near a feshbach resonance. *Phys. Rev. A*, 86:022703, Aug 2012.

[31] L. Landau. Zur theorie der energieubertragung. ii. *Physikalische Zeitschrift der Sowjetunion*, 2:46–51, 1932.

[32] Clarence Zener. Non-adiabatic crossing of energy levels. *Proceedings of the Royal Society of London A: Mathematical, Physical and Engineering Sciences*, 137(833):696–702, 1932.

[33] Marko Cetina, Michael Jag, Rianne S. Lous, Jook T. M. Walraven, Rudolf Grimm, Rasmus S. Christensen, and Georg M. Bruun. Decoherence of impurities in a fermi sea of ultracold atoms. *Phys. Rev. Lett.*, 115:135302, Sep 2015.